

Highlights

1. Four Quaternary slope failures with area of $\sim 11,000 \text{ km}^2$ and volume of $\sim 1035 \text{ km}^3$ are identified in SCS;
2. The studied MTDs are not directly sourced from slopes built on major deltaic depositional systems;
3. The slope is a giant debris flow corridor that has transected broad subsided continental margin;
4. The coarse-grained sediments are an important component for the occurrence of slope failures;
5. The proposed lithostratigraphy on slope stability is useful for other continental margins.

Reconstruction of repeated Quaternary slope failures in the northern South China Sea

Qiliang Sun^{a,b,c,*}, Joe Cartwright^d, Xinong Xie^{a,c}, Xiangyang Lu^{a,c}, Shengqiang Yuan^e,
Chuanxu Chen^f

^a*College of Marine Science and Technology, China University of Geosciences (CUG), Wuhan, Hubei 430074, PR
China;*

^b*Laboratory for Marine Mineral Resources, Qingdao National Laboratory for Marine Science and Technology,
Qingdao 266061, China;*

^c*Key Laboratory of Tectonics and Petroleum Resources, China University of Geosciences, Ministry of Education,
Wuhan 430074, China;*

^d*Department of Earth Sciences, University of Oxford, Oxford OX1 3AN, England;*

^e*Research Institute of Petroleum Exploration & Development, PetroChina, Beijing 100083, China;*

^f*Sanya Institute of Deep-sea Science and Engineering, Chinese Academy of Sciences, Sanya 572000, China*

Abstract

A series of Quaternary mass transport deposits (MTDs) with a total areal extent of $\sim 11,000 \text{ km}^2$ and a conservative volume estimate of $\sim 1035 \text{ km}^3$ are observed in the Pearl River Mouth Basin (PRMB), northern South China Sea (SCS), based on integrated analysis of extensive 2-D/3-D seismic data, multibeam bathymetric data and ODP/IODP wells. Unlike other large MTDs worldwide, the MTDs in this study are not directly sourced from slopes built on major deltaic depositional systems. Moreover, they are remarkable in that the whole PRMB is a giant debris

*Corresponding author: Dr. Qiliang Sun
Telephone/fax: +86 27 67886167
E-mail address: sunqiliang@cug.edu.cn.

flow corridor that has transected a broad subsided continental margin. The MTDs in this study have a large evacuation zone on the slope and a depositional zone in the ocean basin connected by a narrow pathway. Six events of MTDs (MTDa - MTDD on the slope and MTDo1 - MTDo2 in the ocean basin) have been identified as being separated by basal erosional surfaces defined by strong negative seismic reflections. Similar ages and volumes (depleted volume of MTDb on the slope and the depositional volume of MTDo2) suggest that MTDo1 and MTDo2 correlate with MTDa and MTDb, respectively. The major factor controlling the occurrence of slope failures is argued to be the presence of a key reflection package. This package is interpreted to consist of gas-charged, coarse-grained sediments deposited during a relative lowstand of sea level, overlain by a unit of fine-grained sediments. Other contributing factors that influenced the morphology and position of the MTDs include the presence of free gas, normal faulting in the slope sediments, and seafloor relief related to igneous activity. From MTDD to MTDb, slope failures are shown to have retrogressed upslope with a decreasing time interval between events. The events, dimensions, susceptible factors and formation processes of slope failures in the study area are demonstrated for the first time in the petroliferous basin of northern SCS. Their recognition is important for geo-hazard assessment (e.g. tsunami) in this area. Moreover, this study highlights that the lithostratigraphy of the slope succession, especially the coarse-grained sediments in the deepwater area, can be an important component for the occurrence of slope failures, and may be a key factor in slope stability on other continental margins too.

Keywords:

Slope failures, mass transport deposits (MTDs), debris, canyons, sediment corridor, free gas,

South China Sea

1. Introduction

Mass transport deposits (MTDs) resulting from slope failures are an assemblage of remobilized sedimentary units which are redeposited on the seafloor (slope and ocean basin) (e.g. [Nardin et al., 1979](#); [Hampton et al., 1996](#); [Canals et al., 2004](#)). They have been extensively documented in continental slope and oceanic basin floor settings using geophysical data (e.g. seismic, multibeam bathymetry and well logging) and core/field observation (e.g. [Piper et al., 1985, 1997](#); [Moscardelli et al., 2006](#); [Tripsanas et al., 2008](#); [Alves and Cartwright, 2009](#); [Armitage et al., 2009](#); [Bull et al., 2009](#); [Strasser et al., 2011](#); [Dugan, 2012](#); [Jackson et al., 2012](#); [Gamboa and Alves, 2016](#)). Most studies of MTDs are focused on the descriptions of geomorphological and lithological characteristics and the understanding of their causal mechanisms. Slope failure is a serious geo-hazard, so it is important to reconstruct their history, especially in the regions where the occurrence of MTDs is frequent and there are huge population along the coastlines (e.g. offshore Norway, North Sea, Mediterranean Sea, offshore West Africa, offshore Brazil, Gulf of Mexico and South China Sea) and where there are susceptible marine infrastructures (e.g. submarine cable and drilling platforms).

Although MTDs occur in diverse environments, the largest ($>10^5$ km²) are commonly found associated with the slopes of large Cenozoic deltas (e.g. Amazon, Indus, Nile and Mississippi Deltas) ([Piper et al., 1997](#); [Calvès et al., 2015](#); [Omeru and Cartwright, 2015](#); [Obelcz et al., 2017](#)). Recently, many studies have explored the formation processes of MTDs based on observations using modern multichannel seismic data (e.g. [Bryn et al., 2005](#); [Lamarche et al., 2008](#); [Sawyer et](#)

al., 2009; Joanne et al., 2010; Strasser et al., 2011; Jackson, 2012; Omeru and Cartwright, 2015).

Uncertainties in reconstructing the formation processes of MTDs, especially for multi-stage MTDs, are usually difficult to constrain and a large database is needed to make the results precise.

In this study, several distinctive MTDs are mapped and described over an area extending to $\sim 11,000 \text{ km}^2$ with a conservative volume of $\sim 1150 \text{ km}^3$ are investigated. This study is based on an extensive coverage of 2-D/3-D multichannel seismic data, multibeam bathymetrical data and correlation with two ODP/IODP wells. The study is aimed at: (1) Characterizing MTDs and their depositional frameworks, (2) identifying and dating the main events of slope failures, (3) calculating their dimensions (areas, thicknesses and volumes), (4) analyzing the susceptible factors and triggers, and (5) reconstructing their initiation, propagation and depositional processes.

2. Geological setting

2.1. Geological and depositional evolution of PRMB

The SCS is the largest and deepest marginal sea in the western Pacific (Fig. 1) and it experienced complex tectonic evolution during the Cenozoic (e.g. Lüdmann and Wong, 1999; Yan et al., 2001; Xie et al., 2006; Sun et al., 2008; Sibuet et al., 2016). It was formed by seafloor spreading during late Oligocene to early Miocene (Briais et al., 1993; Taylor and Hayes, 1983) and drifted to its present position in the middle Miocene (Briais et al., 1993; Hall, 2002).

The PRMB in which the studied slope failures are located covers an area of $200,000 \text{ km}^2$ and lies in the central part of northern SCS (Fig. 1). It is one of several Cenozoic rift basins and evolved through a Late Cretaceous-early Oligocene rifting stage, a late Oligocene-early Miocene transition stage and a middle Miocene-present subsidence stage (e.g. Ru and Pigott, 1986; Yu,

1994; Gong and Li, 1997; Xie et al., 2006). In the Cenozoic, three main tectonic episodes, the Zhuqiong Event, the Nanhai Event and the Dongsha Event, occurred in the PRMB (Fig. 2) (Lüdmann and Wong, 1999; Pang et al., 2008; Dong et al., 2009). The latest Dongsha Event started in the late Miocene (~10.5 Ma) and lasted until present day (Fig. 2) (Lüdmann and Wong, 1999). It mainly caused basement uplifting and faulting around the Dongsha Islands (Lüdmann and Wong, 1999; Lüdmann et al., 2001).

In response to the structural evolution of the PRMB, the sedimentary environments/processes can be divided into three stages. The Paleogene to lower Oligocene strata comprise fluvial-lacustrine sediments in discrete rifts, which include an Eocene source rock (dark lacustrine mudstone) (Fig. 2) (e.g. Gong et al., 1989; Gong and Li, 1997; Zhu et al., 2009). The upper Oligocene strata are transitional (coastal and littoral) facies and serve as both source rocks and reservoirs (Zhu et al., 2009). Marine facies sediments started to dominate the PRMB since Neogene during which period the sea level gradually rose (Gong et al., 1989; Zhu et al., 2009). The shelf break zone of the northern SCS was ~100 km south of the present seabed break before 23.8 Ma, migrated northwards from 23.8 Ma to 21.0 Ma and has been stable in its present location since 21.0 Ma (Liu et al., 2011). Migrating canyons have developed in the upper slope since middle Miocene and are related to the interaction of alongslope bottom currents and downslope turbidity currents (Zhu et al., 2010). These canyons served as pathways for sediments transported from the Pearl River Delta and shelf to deep water (Gong et al., 2008; Zhu et al., 2010). Coarse-grained sediments (sand-to-silt) interbedded with fine-grained sediments characterized the study area from middle Miocene to late Pliocene (Gong and Li, 1997; Wu et al., 2015). Fine-grained sediments dominated the depositional regime in the deep-water area of PRMB since

the Pleistocene (Gong and Li, 1997; Wang et al., 2000). Shallow gas transported from deep strata through gas chimneys, normal faults and mud diapirs were also observed around the toe zone of canyons where a large gas field (Liwan gas field) was located (Sun et al., 2012).

2.2. Previous slope failure studies in the PRMB

The MTDs in the PRMB have been investigated in several previous studies (Sun et al., 2008; Li et al., 2014; He et al., 2014; Wang et al., 2014, 2017; Sun et al., 2017a, 2017b, 2018). About 77 canyon-related MTDs with small sizes (0.53-18.09 km²) were identified in the slope canyon zone and their formation is related to the steep slope and the rheological behavior of failed sediments (He et al., 2014).

A large-scale product of slope failure named as the Baiyun Slide (In this study, we use the nomenclature of “mass transport deposit (MTD)” to represent the product of slope failure) was identified in the slope region of the PRMB (Sun et al., 2008). Limitations of the available datasets meant that the characteristics of the Baiyun Slide were not correctly identified and the coverage of the Baiyun Slide was greatly overestimated (estimated areal extent was ~13,000 km² on the slope (Sun et al., 2008) and the actual area in the slope region is ~5500 km² documented in this study). Based on seabed morphologies observed from the bathymetric data, development phases and slide areas of the Baiyun Slide were subdivided by Li et al. (2014b) and Wang et al. (2014), respectively. For a simple slope failure which forms through single failed event, it is probably valid to use the seabed morphologies (bathymetrical data) to deduce the formation processes. However, the Baiyun Slide covers an area of ~5500 km², has a maximum length of ~200 km (excluding the ocean part) and has complex internal structures (Figs. 3-4). Therefore, though some

of their observations and conclusions are valid, many of them are controversial. [Wang et al. \(2017\)](#) investigated the upper part (head zone) of the Baiyun Slide and stressed that the topography of MTDs likely influenced the distribution of post-MTDs turbidites. The volumes of the Baiyun Slide, especially the volume of turbidites generated by slope failure and the volume of shear compaction during failed sediment emplacement, were calculated, based on the seabed escarpment restoration and best-fit curves of porosities of MTDs and 'background' slope sediment ([Sun et al., 2018](#)). The original volume of failed sediments is ~18% higher than the volume calculated from seismic data (used in this study) ([Sun et al., 2018](#)).

Free gas which is trapped within the basal zone of MTDs is documented by [Sun et al. \(2017a\)](#). After the emplacement of MTDs, failed sediments (overconsolidated through lateral shear) usually act as a seal and obstructed the vertical fluid flow ([Sun et al., 2017a, 2018](#)). However, lateral fluid flow along the basal zone may trigger new slope failure (retrogressive slope failure) ([Sun et al., 2017a](#)). The timing of the MTDs is also debated in [Li et al. \(2014\)](#) and [Wang et al. \(2014\)](#). The Baiyun Slide is estimated to occur at ~0.3 Ma and ~10.5-5.5 Ma respectively, based on the variable sedimentation rates ([Wang et al., 2014; Li et al., 2014](#)). Three individual MTDs are clearly identified based on their anatomy on high-resolution 3-D seismic data ([Sun et al., 2017b](#); See [Frey Martinez et al. 2006](#), and [Bull et al. 2009](#) for diagnostic features of MTDs on seismic data). Their ages were estimated to be ~0.54 Ma, ~0.79 Ma and ~1.59 Ma, respectively, from an albeit long-range seismic correlation with ODP Site 1146 by [Sun et al. \(2017b\)](#). However, that previous study was only focused on the 3-D seismic survey located in part of the eastern scarp and did not extend to a full description and analysis of the characteristics and formation processes of the Baiyun Slide.

This study addresses a series of primary questions regarding the Baiyun Slide, such as: 1) the individual MTD events, 2) the relationship between distinct event, 3) the evacuation and depositional zones of MTDs, 4) the dimensions (area, thickness and volume) and flow direction of each event, and 5) the formation processes of each event. These are open questions that are tackled in this study.

3. Data and methods

3.1. Datasets

The seismic data used in this study comprises 35,200 km 2-D seismic data with line spacing ranging from 2 km to 8 km on the slope and 8-16 km in the ocean basin and ~6750 km² 3-D seismic data (Fig. 3a). The two 3-D seismic surveys were collected in 2006 located along the eastern scarp of MTDs) and in 2008 located in the head zone of the MTDs (Fig. 3a). These surveys were acquired with 3000 m long streamers (6 streamers with spacing of 12.5 m) consisting of 240 channels at a spacing of 12.5 m and an array of tuned air guns with a total volume of 160 inch³ using a shot interval of 25 m (Sun et al., 2017a). They have a vertical resolution of ~9 m calculated from main frequency of ~45 Hz and strata velocity of ~1540 m/s from ODP site 1146 and lateral resolution of 12.5 m. Most of the 2-D seismic lines (Figs. 3c-d, 5c, 6d-f, 7f, 9d-e) presented in this study were acquired in 1999-2002 with a 3000 m long 120-channel streamer and a hydrophone group interval of 25 m and a sampling interval of 4 ms. The main frequency is of ~35 Hz and thus a vertical resolution is ~11 m. The additional seismic lines presented in Fig. 7e and Fig. 8d were collected in 1987 with 2000 m long 48-channel receiver array and Fig. 5d was collected in 1986 with 1500 m long 48-channel receiver array. They have a

vertical resolution of ~13 m.

About 37,500 km² multibeam bathymetrical data are used in this study. It was acquired in 2008 by a SeaBeam 2112 multibeam echo-sounder which operates at a main frequency of 12 kHz with a pulse length of 3-20 ms (Wang et al., 2014). The depth accuracy is better than 0.5% of the water depth and full bathymetric swath width comprises 120° (Wang et al., 2014). Vertical and horizontal resolutions are 3-6 m and 100 m, respectively, which allowed us to identify and analyse the seabed morphologies in detail. The bathymetric maps (Figs. 1, 3, 6a-c, 7a, 8a, 9a) used in this study were made using Global Mapper[®] 14.0 and Surfer[®] 12.0.

ODP Site 1146 (19°37.40'N, 116° 16.36'E) and IODP Site U1432 (18°21.08'N, 116° 23.45'E) are used in this study (Fig. 3a). The former with well depth of 607 m was drilled in 1999 in a water depth of 2091.1 m (on the slope) and the latter drilled in 2014 was located in the ocean basin with a water depth of 3829 m and well depth of 110 m. ODP Site 1146 is ~46 km to the east of the repeated MTDs and is used to estimate the ages of MTDs through the synthetic seismogram (Sun et al., 2017b). An interval velocity of 1540 m/s, which is extracted from shallow strata of ODP Site 1146, is used for time-to-depth conversion in this study. IODP Site U1432 located in the southeastern region of MTD02 drilled through sediments younger than 1.0 Ma BP and no well logs are available for this site. Sedimentation rate used for calculating the ages of MTDs (MTD01 and MTD02) and lithological calibration of the MTDs in this study come from this borehole.

3.2. Methods

The standard interpretation workflow involved a systematic examination of the seismic data to interpret, describe and analyze the seismic features regarded as diagnostic of MTDs, using

standard criteria (e.g. [Bull et al., 2009](#)). The biostratigraphic ages from ODP Site 1146 were linked to the seismic reflections through the synthetic seismogram (for details see [Sun et al., 2017b](#)) and then correlated into the 3-D seismic survey where MTDs occurred. The bases and tops of MTDs were mapped and traced from the high-resolution 3D seismic surveys where identification is more easily achieved and then correlated into the 2D seismic surveys. Their bases and tops usually have high-amplitude continuous negative and positive seismic reflections ([Fig. 5a](#)) which simplifies the correlation from the 3-D seismic surveys to the 2-D seismic surveys.

For the MTDs (MTDa, MTD_{o1} and MTD_{o2}) whose ages can not been directly correlated by the ODP/IODP wells, local sedimentation rate (Sr) and overlying sediment thickness (St) (from top of MTDs to seabed) are used to estimate their ages (A). Their ages are estimated from the equation:

$$A = \frac{St}{Sr} = \frac{T \times V}{2 \times Sr} \quad (1)$$

Where T is the two way travel time in unit of second (s) and V is the strata velocity in unit of m/s. The age errors are mainly caused by seismic resolution and they are estimated to be no more than one seismic event, e.g. <10 m on the slope (average value of ~9 m and ~11 m) and <13 m in the ocean basin. To avoid the influence of MTD_{o1}, the strata thickness of normal deposition above MTD_{o2} is calculated far from MTD_{o1}.

4. Results

4.1. Seabed morphologies and subsurface structures

4.1.1. Slope canyons and free gas

About 17 slope canyons with widths ranging from 2.1 to 5.3 km and depths between 50 and 360

m (measured in the middle of these structures) are observed in the upper slope (Figs. 3, 4a-5b). They have been laterally migrating eastwards since the middle Miocene (surface T₃) and are the result of the interaction of down-slope (turbidity current) and along-slope (contour current) processes (Zhu et al., 2010). The slope canyons serve as important pathways for sediment transport from the shallow-water shelf/delta to the deep-water area.

Enhanced seismic reflection anomalies interpreted as shallow gas (e.g. Judd and Hovland, 2007; Sun et al., 2012) are widespread in the northern scarp of the slope failure (Fig. 3b) where free gas migrated into the strata of middle Miocene to Recent age (Fig. 4b). In the eastern scarp, the free gas is just located underneath the MTDs (Sun et al., 2017a) in the layered coarse-grained sediments of lower slope (Figs. 4c-d, 5c) and within the strata above igneous complexes (Figs. 4c-d) or along normal faults (Figs. 4c, 7c).

4.1.2. Escarpment and scarps

A multifaceted seafloor escarpment that comprises a series of arcuate scarps is interpreted to result from slope failure (Figs. 3, 4d, 7c-7e, 8b). In its northern part, it nearly extends W-E and cuts the toes of inter-canyon ridges. It changes orientation and strikes NW-SE in its middle and southern parts. In general, the dips and heights of the escarpment become steeper (5°- 16°) and higher (~50 - ~200 m) from the lower slope to upper slope (Fig. 3). The escarpment is not clearly identified in its lower left part (to the west of the Central Valley) (Fig. 3b) and the delineation in this part is drawn, mainly based on the subsurface MTDb (Fig. 5c).

4.1.3. Seabed troughs and valley

Seabed troughs (small scale) and a large scale erosional feature, here named the Central Valley (to distinguish it from the slope canyons) are identified in the middle and lower slope (within the

escarpment of MTDs) (Figs. 3, 4c, 5c). In the middle slope, these structures (troughs) originate beyond the escarpment to the west or are directly connected with the canyons to the north. Their maximum width and depth are 3 km and 50 m, respectively. The west-east oriented troughs (from the western escarpment) join with the northwest-southeast orientated troughs and finally feed into the Central Valley on the lower slope (Fig. 3) which has a length of ~85 km, widths of 3 - 8 km and depths of 18 - 60 m, respectively. The Central Valley mainly extends NW-SE and terminates into the ocean basin (Fig. 3).

4.1.4. Igneous complexes

Three large igneous complexes comprising extrusions (seamounts) and intrusions and some small-scale igneous intrusions which have similar seismic characteristics to those documented by Sun et al. (2014) and Fan et al. (2017) are identified (red ellipses in Fig. 3b; Figs. 4c-d, 5c, 6d, 7e-f, 8d, 9e). The seamount in the lower slope has a relief at the seabed of ~475 m (Figs. 3b, 9e) and the igneous complexes in the middle slope have positive reliefs of ~80 - 180 m (Figs. 3b, 8d). The strata above or around the igneous intrusions are deformed and forced fold structures are observed (Figs. 4c-d, 8d, 9e). Onlap seismic reflections are also observed at the flanks of igneous complexes. Sometimes, the stratal deformation nearly reaches up to the seabed or to the bases of the MTDs (Figs. 4c-d). Normal faults and associated fluid flow occur within the strata just above deep igneous complexes (Fig. 4c).

4.1.5. Continent ocean boundary

A linear positive relief feature (here named as continent-ocean boundary (COB) from Taylor and Hayes (1983)) separates the PRMB from the deep ocean basin (Fig. 3). It demarcates the ocean basin to the south with an elevation difference of ~1100 m, and the depression (mini-basin)

to the north with an elevation difference of ~250 m. The COB is composed of a basement high (igneous complexes) and a sediment drape (Figs. 5d, 7f). Onlap onto this feature is observed along the northern flank of COB (Figs. 5c, 7f). A narrow (~25 km width) and deep (~450 m from the top of COB) gap in this ridge (here named as neck of COB) connect the PRMB and the deep ocean basin and transects the entire COB structure (Fig. 3). It mainly strikes NW-SE but re-orientates to nearly N-S in its southern part.

4.1.6. Turbidites infilling the depressions

High-amplitude seismic reflections with moderate-high continuity infill the depositional accommodation (depressions) and onlap seismic reflections can clearly be observed in the flank of the depression (Figs. 4b-d, 5c, 6d-f, 7e-f, 8d, 9d-e). They are interpreted as coarse-grained turbidites probably sourced from paleo-Pearl River Delta (Gong and Li, 1997; Wu et al., 2015). In the lower slope (mini-basin), the thickness of coarse-grained turbidites reaches up to ~350 m and its lowermost portion just onlaps onto the surface T₃ (Figs. 7f, 9e). Locally, extremely high amplitudes are observed (Figs. 5c, 9d), probably related to gas migration into these sediments, according to the diagnostic features (e.g. reversal polarity, stacked seismic anomalies and low frequency) documented by Judd and Hovland. (2007), Løseth et al. (2009) and Brown (2011). Towards the upper slope, the coarse-grained turbidites gradually wedge out (Figs. 7f, 8d, 9d). In the middle slope, onlapping seismic reflections onto the eastern and western slopes are also observed. However, their lowermost portion terminates at the younger surface T₂ (Fig. 7e). Thick weak seismic reflections with high continuity overlay the coarse-grained sediments (Figs. 7f, 9d-e) and they are probably composed of fine-grained sediments, judging from the lithological calibration of ODP/IODP wells (Wang et al., 2000; Expedition 349 Scientists, 2014). Their bases

are commonly coincident with the basal surfaces of MTDs (Fig. 9e).

4.2. Slope failure events and timings

Four MTDs (from young to old, MTDa - MTDd) are identified on the slope of the PRMB and they are separated by strong negative seismic reflections (basal surfaces) (Fig. 5c). From the seismic correlation with ODP Site 1146, they are dated at ~0.54 Ma (MTDb), ~0.79 Ma (MTDc) and ~1.59 Ma (MTDd), respectively (for details see section 4.2 and Sun et al. (2017b)). MTDa do not extend into the 3D seismic survey used by Sun et al. (2017b) and therefore a local sedimentation rate is used to estimate the age of MTDa. According to the sedimentation rate of 122 m/Ma in the study area (Xie et al., 2013) and the drape of ~23 m, MTDa is estimated to be ~0.19±0.08 Ma, which is slightly older than the estimated age of ~0.18±0.08 Ma, based on the sedimentation rate of ~130 m/Ma from ODP Site 1146.

Two events of MTDs (MTDo1 and MTDo2) are recognized across the COB in the ocean basin. They are characterized by an opaque or reflection free seismic facies (Fig. 5d). Compared to the areal extent of MTDo2 of ~5602.72 km², MTDo1 is much smaller, having a limited areal extent of ~256.31 km² (Table 1) and being located immediately next to the neck of COB (Fig. 6a). The strata above MTDo1 and MTDo2 are ~25.2 m and ~63.6 m thick, calculated from their upper boundaries to the present day seabed. Based on the sedimentation rate of ~120 m/Ma from IODP U1342 (Expedition 349 Scientists, 2014, Fig. 5b), the MTDo1 and MTDo2 are dated as ~0.21±0.11 Ma and ~0.53±0.11 Ma, respectively.

4.3. Detailed characteristics of MTDs

4.3.1. MTDa

MTDa is the smallest of the four MTDs on the slope (Table 1) and is characterized by chaotic/blank seismic reflections in which short laterally discontinuous seismic reflections are observed (Figs. 4c, 5b, 6e-6f). MTDa is located just upslope of the neck of COB and mainly elongated along the Central Valley (Fig. 6a). To the west, MTDa is bounded by the burial scarp which is linear and ranges from 115 to 136 m (Figs. 4a, 5c). To the east, it shares the same boundary with the present Central Valley (Fig. 5c) and gradually wedges out towards to the COB in the south (Fig. 6e). Next to the COB, MTDa overlapped onto the COB to the south (Fig. 6f). Older MTDs (MTDb and MTDd) are intensely eroded by MTDa and they are separated by a strong negative seismic reflection (Fig. 5c). MTDa has two depocenters and both have similar positions with respect to the Central Valley (Fig. 6a). The residual volume of MTDa is $\sim 22.2 \text{ km}^3$ (Table 1).

4.3.2. MTDb

MTDb is the largest amongst the four MTDs on the slope (Table 1). It covers a total area of $\sim 5500 \text{ km}^2$ including $\sim 3166 \text{ km}^2$ residual area and $\sim 2334 \text{ km}^2$ total evacuation area which is mainly located in the eastern and northern parts of MTDb and has a steeper escarpment from the lower slope to upper slope (Fig. 7a; Table 1). It extends east-west in the northern part (head zone) and turns to northwest-southeast in the middle and lower parts (Fig. 7a).

In its northern part, arcuate scarps of MTDb directly cut through the toes of migrating canyons. Normal faults which usually restrict the locations of scarps (southern and northern scarps) are frequently observed in the northern part (head zone) (Fig. 7b). They usually develop at the flanks of underlying basement structures and free gas is observed along the faults (Fig. 7c). Linear

grooves formed by the erosion of transported blocks (e.g. Posamentier and Kolla, 2003; Moscardelli et al., 2006) are observed in its basal surface in the head zone. They extend from the western scarp (headwall) eastwards and join with the NW-SE grooves originating from the northern scarp (Figs. 7b, 7g). The grooves indicate the flow directions of failed sediments from their source area and are hence useful as kinematic indicators of the transport direction (e.g. Bull et al., 2009). Some of the failed sediments accumulated against the northern scarp and form an average ~58 m thick depocenter (Fig. 7a). Most of the failed sediments were transported downslope, judging from the high scarps and erosional grooves (Figs. 7b-d).

In the middle slope, MTDb is thin and has a limited distribution (Fig. 7e). In the lower slope, MTDb is thick in the western part and it completely disappears in the eastern part (Fig. 7a). An elliptical depocenter with maximum thickness of ~110 m (143 ms twt) is observed along the western boundary of MTDb. In this area, the MTDb deeply erodes into the underlying strata (until T_1) with sharp boundaries (Figs. 4c, 5c, 9e). At the northern part of the depocenter, MTDb is strongly eroded by the young slope failure (MTDa) (Fig. 6d) and form arcuate scarps at the seafloor (Fig. 6b). It flows over the steep scarp which bounds MTDa and deposits within the sediment fairway (Central Valley) (Fig. 7f, 9e). In the sediment fairway, the underlying MTDD is eroded by MTDb (Fig. 5c).

4.3.3. MTDc

MTDc is mainly located along the eastern escarpment extending NW-SE, has a length of ~55 km and a width of ~13 km in its central part (Fig. 8a). It is bounded by the igneous complexes and eastern escarpment to the north and east, respectively (Figs. 8a, 8d). Its western part is strongly eroded and bounded by the eastern flank of Central Valley (Fig. 5c). Moreover, it wedges out to

the south (Fig. 8d) and it is about ~28 km away from the neck of COB (Fig. 3b). The head wall of MTDC is not directly observed. A sudden slope change (from ~0.78° to ~1.15° in Fig. 8c) where igneous complexes occur (local dip at the south flank of igneous complexes reaches up to 25°) is observed just to the north of MTDC (Figs. 8a, 8d). Towards the igneous complexes, the coarse-grained sediments just underneath the MTDC onlap onto the underlying strata and become thinner (Fig. 5d). A number of acoustically 'soft' seismic reflection anomalies which are interpreted as being due to the presence of free gas (Loseth et al., 2009) are also observed (Fig. 5d). The depocentres of residual failed sediments are against the eastern escarpment which is composed of five arcuate scarps (Fig. 8b). Tilted blocks are observed within the scarp where the depocenter is located. Linear structures which are from the upper part of MTDC or from the scarps are also observed and they are usually parallel to the scarps and extend downslope (Fig. 8b).

4.3.4. MTDD

MTDD is mainly located in the lower slope and its southern part is connected to the neck of the COB (Fig. 3b). It is bounded by a linear burial scarp to the west and its main body extends NW-SE (Figs. 9a, 9e). Its eastern boundary is roughly along the present escarpment (Fig. 9a). Towards the north, the seabed becomes steeper (from ~0.6° to ~1.1°) and MTDD gradually wedges out (Figs. 9b-d). An arcuate structure is observed in the slope dip transition (change) zone (Fig. 9a). MTDD is overlain by younger MTDs (MTDa - MTDC) and strong negative seismic reflections separate them. This is interpreted as indicating that MTDD is eroded by the younger MTDs (Figs. 4a, 5c, 6f, 9d-e). High-amplitude seismic reflections (coarse-grained sediments) also onlap onto the underlying strata and wedge out towards the upslope region (Fig. 9d). Some high reflections are extremely enhanced, also interpreted as indicating the presence of free gas. Two depocenters

are observed (Fig. 9a). One is located in its upper part and the other is just outside the neck of COB (Fig. 9a). MTDD has a residual volume of $\sim 81.37 \text{ km}^3$ and covers an area of $\sim 832.5 \text{ km}^2$ with average thickness of $\sim 97.74 \text{ m}$ (Table 1).

4.3.5. MTD01 and MTD02

MTD01 is located just downslope of the neck of COB and is circular in outline with its main thickness accumulating within its eastern region (Fig. 6a). MTD01 is visible as a blank or opaque seismic facies that wedges out radially from its depocenter (Figs. 5d, 6a). MTD01 covers an area of $\sim 256.31 \text{ km}^2$ and has a volume of $\sim 12.33 \text{ km}^3$ (Table 1).

MTD02 is the largest in the study area, extending over an area of $\sim 5603 \text{ km}^2$ with an average thickness of $\sim 100 \text{ m}$ and a conservatively estimated volume of $\sim 617 \text{ km}^3$ (Table 1). MTD02 has a classically fan-shaped planform, originating upslope from the neck of COB and is marked by a low seafloor gradient ($\sim 0.05^\circ$) (Fig. 7a). Its maximum thickness of $\sim 112 \text{ m}$ is measured immediately downslope of the neck of COB and it wedges out distally from the neck over a distance of $\sim 65 \text{ km}$ (Fig. 7a). Troughs or grooves are also observed along its base (Fig. 5d), which indicates the MTD02 still has a strongly erosive ability in the ocean part. Like MTD01, MTD02 is also characterized by an opaque seismic facies and both these deposits are interpreted as debris fans, according to the diagnostic features documented by Nardin et al. (1979) and Hampton et al. (1996).

5. Discussion

5.1. Links between MTDs in the slope and ocean basin

The MTDs mapped in the slope domain (MTDa - MTDD) or in the ocean basin domain

(MTDo1 - MTDo2) can be confidently subdivided stratigraphically through their superimposed relationships and clear basal surfaces (strong negative seismic reflections) (Figs. 5a, 5c-d). However, it is difficult to correlate MTDs between the slope and ocean basins using the seismic data, because there is no continuity of reflections across the high and steep COB (~1100 m standing above the ocean basin with slope reaching up to 25°) where most of sediments bypass rather than accumulate. The observations that (1) both MTDo1 and MTDo2 exhibit fan-like planforms with an origin at the neck of COB and (2) consist of a large volume of remobilized sediments suggest that they are sourced from the slope region and are probably related to two of the four MTDs there.

The homogenous seismic reflections of MTDo2 suggest that it is probably linked to a single slope failure event. This argument does not exclude that older MTDs were remobilized again by cannibalization during younger events and mixed into the MTDo2. Considering (1) the large evacuation zone (escarpment) of MTDb on the slope and large deposition volume of MTDo2 in the ocean basin and (2) the similar ages (~0.54 Ma of MTDb and ~0.53±0.11 Ma of MTDo2), MTDo2 and MTDb are interpreted as direct correlatives, and were the result of the same slope failure event or shortly spaced in time. MTDb could be regarded as mainly being the residual material deposited on the failure surface as it propagated in the upslope region and MTDo2 is the depositional segment which was funneled downslope through the neck of the COB. This event remobilized a conservative volume of ~839 km³ (~222.03 km³ on the slope and ~616.69 km³ in the ocean basin). By a similar argument, MTDo1 and MTDa are also interpreted as one single slope failure event which originated from a small area in the slope.

5.2. Preconditioning factors and triggers

434 The large database used in this study and associated detailed interpretation provide an
 435 opportunity to analyse the preconditioning factors and triggers of slope failures in the study area.
 436 The strata in the study area are characterized by a particular depositional pattern in which middle
 437 Miocene-to-early Pleistocene coarse-grained turbidites (porous 'reservoir' layer) are overlain by
 438 fine-grained sediments (low permeability (seal) layer) of Pleistocene to Recent age (above surface
 439 T_0) (Figs. 7f, 9d-e, 10-11) (for details see sections 2.1 and 4.1.5). Moreover, this depositional
 440 pattern is mainly controlled by the location of Pearl River Delta and the relative sea-level change
 441 (Pang et al., 2008), and slope canyons provided the pathway for sediment transportation from
 442 shelf/delta to deep-water area (Zhu et al., 2010). It seems probable that sediments preferentially
 443 accumulated in the mini-basin judging from the stacked onlap seismic reflections (Figs. 4c, 5c, 6f,
 444 7f, 9e). Furthermore, the charge of free gas from deep strata (biogenic and/or thermogenic origins)
 445 into the porous strata (Figs. 4b, 5c, 9d) may have led to development of overpressure in the
 446 transition zone from porous to overlying low permeability layers, leading to the formation of a
 447 weakened layer (Fig. 11). The weak layer could have been the locus for low shear strength and
 448 thus the preferred site for shear failure to occur (e.g. Sultan et al., 2004). Free gas would also have
 449 migrated stratally updip along the porous strata. It possibly leaked to the seabed along the faults
 450 and/or from the tips of porous layers, commonly at the flank of igneous bodies (Figs. 7f, 8a, 8d, 9d,
 451 11). In such an inherently unstable context, the slope would be likely to fail under certain triggers,
 452 such as earthquake-induced deformation (e.g. Nardin et al., 1979; Hampton et al., 1996; Biscontin
 453 et al., 2004). Besides the depositional pattern and free gas charge, the slope gradient increase
 454 which possibly resulted from locally magma intrusion/extrusion may be also increase the
 455 susceptibility of slope instability (Fig. 10) and a slope angle of $>1^\circ$ will greatly increase the

possibility of slope failure (Nardin et al., 1979; Masson et al., 2006; Owen et al., 2007). Since MTDC and MTDd deformed the Pleistocene strata and directly overlie high porosity sediments, the susceptible factors discussed above are probably responsible for the occurrences of these two MTDs.

A series of tectonic depressions and adjacent massifs combine to form the fundamental geometrical framework of the PRMB since the Miocene (Figs. 3a, 11) (Xie et al., 2006, 2014). Many normal faults developed within the flanks of depressions/massifs (Fig. 7c in this study and Fig.12 in Sun et al. (2017b)) and free gas could have utilized these faults to migrate to the shallow strata (Sun et al., 2017b). Normal faults demarcate the southern boundary of MTDb in the head scarp zone (Fig. 7b-c) as well as defining part of its eastern boundary (Sun et al., 2017b). Therefore, normal faults and related free gas maybe also contribute to shaping the limits of the slope failures, especially for MTDb.

Besides the free gas in the porous strata or along normal faults mentioned above, free gas is also widespread around the northern boundaries of MTDb and lower part of slope canyon zone within the middle Miocene-recent strata (Figs. 3b, 4b). Considering the spatial correspondence of free gas and scarps of MTDb, the presence of free gas in sediments close to the incipient failure surface therefore possibly contributed to the slope failure of MTDb (Fig. 11). The slope failures which were proposed to related to high sedimentation rates usually have background sedimentation rates above 100 cm/k.y. (e.g. >100 cm/k.y. of Eastern and Western Debris Flow of Amazon Fan (Piper et al., 1997; Maslin et al., 2005), 650 cm/k.y. of Trænadjupet Slide (Laberg et al., 2003) and >430 cm/k.y. of Nice Slope Failure (Sultan et al., 2004)). The sedimentation rate in the study area is rather low (~6.04 cm/k.y.) (Fig. 10) to lead to shallow overpressure generation and disequilibrium

compaction, may have therefore only have played a limited role in slope failure here.

Actual failure occurs when a susceptible slope is triggered by one or more factors (e.g. earthquake and gas hydrate destabilization) (e.g. Piper et al., 1985; Sultan et al., 2004). Earthquakes are a frequently adopted trigger mechanism since they lead to vertical/horizontal movements which reduce the sediment shear strength allowing failure to occur (e.g. Wright and Rathje, 2003; Martel, 2004). About 103 earthquakes in this intra-plate setting with magnitudes above 5.0 (maximum magnitude of 7.2) have been documented since 1913 close to the study area (CSI, 2017). However, not all earthquakes can trigger slope failures (Pope et al., 2017) and in the cases which are triggered by earthquakes, there also would be delay between earthquake occurrences and slope failure occurrences (e.g. Owen et al., 2007). Considering the earthquakes frequently shake the northern SCS (Fig. 10), they possibly triggered the slope failures in the northern SCS. Igneous activities can also trigger slope failures (Masson et al., 2004) and numerous igneous bodies are identified in this study (Figs. 4c-d, 5c-d). However, onlap seismic reflection configurations at the flanks of igneous bodies (Fig. 5c) show that the igneous activity considerably pre-dated surface T3 (~ 13.8 Ma) (Fig. 5c). This is also verified by the latest study of magmatism in the northern SCS (Fan et al., 2017). Although the igneous activities in this study are unlikely triggers for these slope failures, they led to seabed doming (oversteepening) and subsequently influenced the sedimentation, fault occurrence and fluid flow (Figs. 4c-d, 5c-d, 8d, 9e, 11). In this study, both MTDc and MTDd terminated upslope where the igneous complexes developed (Figs. 4d, 8d, 9e), which suggests the igneous activity mainly contribute as an important preconditioning factor (Fig. 11).

5.3. Reconstruction of slope failures

According to the observations and analysis above, the formation processes of slope failures can be reconstructed approximately over a period beginning from the preconditioning in the middle Miocene to Pleistocene to the emplacement of MTDa more recently (Fig. 12).

Stage I: A seabed topographic framework (depressions surrounded by massifs) similar to the present seabed formed in the PRMB before the middle Miocene (Fig. 12a) (e.g. Gong and Li, 1997; Xie et al., 2014). At this stage, canyons started to develop in the upper slope and the COB was at its present location, and the Pearl River Delta was close to the shelf/slope break (Gong and Li, 1997). Considering the high elevation of the COB, it is reasonable to assume that the neck of the COB also stood proud from the seabed (mini-basin was deeper than the neck of the COB) at this stage. The seabed morphologies were important for the subsequent distribution and occurrence of turbidites and thus for the occurrences of MTDs.

Stage II: This stage lasted from early middle Miocene to early Pleistocene and turbidity currents were active during this stage. Coarse-grained sediments transported via the canyons first passed through the middle slope and deposited into the mini-basin (from surface T₃) (Figs. 6f, 7f, 9e). About 3 Ma later (from surface T₂), they started to infill the accommodation in the middle slope (Fig. 7e). Because the Pearl River Delta moved northwards and the relative sea-level rose (Gong and Li, 1997; Wu et al., 2015), coarse-grained sediments were trapped in the shelf (Gong and Li, 1997) and fine-grained sediments probably dominated in the late part of this stage (from surface T₁). Meanwhile, gassy fluids charged the porous sediments (Figs. 4c, 5a, 5c, 6d, 7f, 9d-e) and gradually migrated upslope (Figs. 10, 12b).

Stage III: Slope failure (MTDd) occurred along the weak layer at the southern flank of

underlying basement highs (igneous complexes) (Fig. 12c), possibly triggered by earthquakes. The headscarp of MTDD was probably eroded by the younger MTDs or by turbidity currents and thus it is not observed at present. For its eastern boundary (lateral scarp), it followed or was slightly west of the present seabed scarp (Fig. 9a). It deeply eroded into the underlying strata in its west flank and formed a steep linear scarp which was also used by younger MTDs (MTDa and MTDb) and Central Valley (Figs. 4c, 5c, 8f, 9d-e). MTDD infilled part of the accommodation in the lower slope. However, it probably did not overflow beyond the neck of COB, though the possibility that MTDD in the neck of COB was completely eroded by the younger MTDb cannot be excluded.

Stage IV: MTDc also occurred at the southern flank of igneous complexes (Figs. 8a, 8d). Its toe zone directly overlays (Fig. 12d) and maybe strongly eroded MTDD, judging from the seismic reflection relationship between them (Fig. 7a). The eastern boundary of MTDc is strictly along the present seabed scarps (Fig. 8a). The arcuate scarps, depocenter and tilted blocks indicated that the lateral failed sediments were importantly as a contribution to MTDc. MTDc probably had a larger extent to the west than its present residual extension and it was eroded by the younger MTDb, based on the observation that its western boundary is immediately along the flank of Central Valley and has a steep slope (Fig. 5c). The topographic effect of igneous complexes possibly protected the MTDc in their lee preventing erosion by younger MTDb, and supported by the interpretation of the wider upper zone (head zone) of MTDc observed in this study (Fig. 8a). The grooves and linear structures in the variance slice suggest the failed sediments mainly flowed to SW (Sun et al., 2017b). However, the transported sediments terminated far from the neck of the COB (Fig. 8a).

Stage V: MTDb was probably formed by a catastrophic slope failure and it had very strong

erosive capability, judging from the large evacuation zone (Fig. 7a), lack of extensional structures in the head zone (Figs. 7c-d) and occurrences of erosional trough and ramp even in the ocean basin (Fig. 5d). It may have formed during a single failure event but more likely through retrogressive failure processes commencing by failure at the toe in the canyon zone with upslope migration of subsequent failures to terminate by cannibalizing upper-left part of MTDb. Other very large MTDs are known to form retrogressively in this fashion, in multiple slip events closely spaced in time (e.g. Storegga Slide, Bryn et al. (2005)). The single or multiple (retrogressive) failure episodes probably occurred over a short time interval, as inferred from the homogeneous seismic reflections of MTDo2 (there are no interfaces identified in MTDo2). The widespread evidence of free gas and normal faults in its head zone (Figs. 4b, 7b-c) probably promoted the occurrence of this slope failure. The slope failure excavated most of the failed sediments in the upper and middle portions and transported them into the ocean floor (Fig. 7a). During this process, the older MTDs (MTDc and MTDd) were eroded and the remobilized sediments (of MTDc and MTDd) mixed with the failed sediments from upslope and were finally transported to the ocean basin through the neck of COB (Fig. 12d). The lower western part of MTDb was located directly against the COB and far from the Central Valley and neck of the COB, which caused a 'harbouring' effect and thus thick residual sediments accumulated in this area (Fig. 7a). The present seabed morphologies, e.g. scarps, probably mainly formed during this stage.

Stage VI: Compared with the three slope failures mentioned above, the youngest slope failure (MTDa) has the smallest size (Fig. 6a; Table 1). From the seabed characteristics, it probably had two sources (Figs. 6b-c): the failed sediments mainly transported along the Central Valley (Fig. 12f) and deposited in the lower slope (mainly within the Central Valley), and the ocean basin (Fig.

6a). MTDa probably also deposited within the neck of the COB and because of low data coverage in this area, it is not identified.

6. Conclusions

Through analysis of large amount of 2-D and 3-D seismic data together with multibeam bathymetrical data and ODP/IODP well data, five main conclusions can be drawn from this study.

1. Four events of MTDs (MTDa - MTDd) on the slope and two events (MTDo1 - MTDo2) in the ocean basin are identified in this study, which are connected each other only through a narrow neck of the COB;

2. The six MTDs formed by four Quaternary slope failures ($\sim 0.19 \pm 0.08$ (0.21 ± 0.11) Ma, ~ 0.54 (0.53 ± 0.11) Ma), 0.79 Ma and 1.59 Ma). MTDo1 and MTDo2 are the depositional parts in the ocean basin of two youngest slope failures which formed corresponding residual MTDa and MTDb on the slope, respectively. The largest slope failure (including MTDb and MTDo2) extends over an area of $\sim 11,000 \text{ km}^2$ and has a conservative volume of $\sim 839 \text{ km}^3$;

3. The emplacements of these MTDs were probably catastrophic with strongly erosive ability with older deposits being eroded by younger ones, which resulted in an evacuated zone on the slope of PRMB and depositional debris fans in the ocean floor;

4. The repeated MTDs (from MTDd to MTDb) retrogressed upslope, commencing from the mini-basin (MTDd) back stepping upslope direction (MTDb);

5. A number of preconditioning factors are identified that rendered the slope susceptible to failure, namely, (1) deposition coarse-grained turbidites and overlying fine-grained low permeability sediments, (2) relative sea-level fluctuation and progradation/retrogradation of Pearl

River Delta, (3) free gas/shallow gas, (4) weakening of slope by normal faults and igneous complexes. Earthquakes are considered to be the likely principal triggers;

This study fully characterizes these Quaternary slope failures for the first time in the most petroliferous basin of northern SCS and reconstructs their formation processes, which will be helpful for the hydrocarbon exploration and geo-hazard assessment (e.g. pipeline and drilling platform) in the study area. This study also highlights the importance of depositional package of coarse-grained sediments and overlying fine-grained sediments on the occurrence of slope failures. Similar depositional package like these documented in this study are widespread in the continental basins worldwide, which possibly interpret the frequent slope failures observed in nearly every continental basin. Finally, this study indicates that the largest MTDs are not necessarily related to/source from discharges of large rivers and shelf deltas. Moreover, large volume of failed sediments could transport downslope as debris flows and it greatly contributes to the deposition in the ocean basin.

Acknowledgements

This work was supported by the National Scientific Foundation of China (Grant Nos. 91528301 and 41676051), the Programme of Introducing Talents of Discipline to Universities (No. B14031) and the Fundamental Research Funds for the Central Universities-the China University of Geosciences (Wuhan) (No. CUG160604). We thank the China National Offshore Oil Company, the Guangzhou Marine Geological Survey and the Second Institute of Oceanography for permission to release the data. Chief-editor Michele Rebesco, Dr. Davide Gamboa and an anonymous reviewer are thanked for their invaluable comments and suggestions, which have

greatly improved this paper. Prof. David J.W. Piper is thanked for his constructive suggestions on the original version of this paper.

References

- Alves, T. M., Cartwright, J.A., 2009. Volume balance of a submarine landslide in the Espírito Santo Basin, offshore Brazil: quantifying seafloor erosion, sediment accumulation and depletion. *Earth Planet. Sci. Lett.*, 288: 572-580.
- Armitage, D.A., Romans, B.W., Covault, J.A., and Graham, S.A., 2009. The influence of mass-transport-deposit surface topography on the evolution of turbidite architecture: The Sierra Contreras, TresPasos Formation (Cretaceous), southern Chile. *J. Sediment. Res.*, 79: 287-301.
- Biscontin, G., Pestana, J.M., Nadim, F., 2004. Seismic triggering of submarine slides in soft cohesive soil deposits. *Mar. Geol.*, 203: 341-354.
- Briaies, A., Patriat, P., Tapponnier, P., 1993. Updated interpretation of magnetic anomalies and seafloor spreading stages in the South China Sea: implications for the Tertiary tectonics of Southeast Asia. *J. Geophys. Res.*, 98: 6299-6328.
- Brown, A.R., 2011. Interpretation of three-dimensional seismic data. 7th Edition. Society of Exploration Geophysicists and American Association of Petroleum Geologists, pp. 665.
- Bryn, P., Berg, K., Forsberg, C.F., Solheim, A., Kvalstad, T.J., 2005. Explaining the Storegga Slide. *Mar. Pet. Geol.*, 22: 11-19.
- Bull, S., Cartwright, J., Huuse, M., 2009. A review of kinematic indicators from mass-transport complexes using 3D seismic data. *Mar. Pet. Geol.*, 26: 1132-1151.
- Calvès, G., Husse, M., Clift, P.D., Brusset, S., 2015. Giant fossil mass wasting off the coast of West India: The Nataraja submarine slide. *Earth Planet. Sci. Lett.*, 432: 265-272.

632 Canals, M., Lastras, G., Urgeles, R., Casamor, J.L., Mienert, J., Cattaneo, A., De Batist, M., Haflidason, H., Imbo,
633 Y., Laberg, J.S., Locat, J., Long, D., Longva, O., Masson, D.G., Sultan, N., Trincardi, F., Bryn, P., 2004. Slope
634 failure dynamics and impacts from seafloor and shallow sub-seafloor geophysical data: Case studies from the
635 COSTA project. *Mar. Geol.*, 213: 9-72.

636 Dugan, B., 2012. Petrophysical and consolidation behavior of mass transport deposits from the northern Gulf of
637 Mexico, IODP expedition. *Mar. Geol.*, 315-318: 98-107.

638 Expedition 349 Scientists, 2014. South China Sea tectonics: opening of the South China Sea and its implications
639 for southeast Asian tectonics, climates, and deep mantle processes since the late Mesozoic. *International*
640 *Ocean Discovery Program Preliminary Report*, 349. <http://dx.doi.org/10.14379/iodp.pr.349.2014>.

641 Fan, C.Y., Xia, S.H., Zhao, F., Sun, J.L., Cao, J.H., Xu, H.L., Wan, K.Y., 2017. New insights into the magmatism
642 in the northern margin of the South China Sea: Spatial features and volume of intraplate seamounts. *Geochem.*
643 *Geophys. Geosyst.*, 18: 2216–2239.

644 Gamboa, D., Alves, T., 2016. Bi-modal deformation styles in confined mass-transport deposits: Examples from a
645 salt minibasin in SE Brazil. *Mar. Geol.*, 379: 176-193.

646 Gamboa, D., Alves, T., Cartwright, J., 2011. Distribution and characterization of failed (mega) blocks along salt
647 ridges, southeast Brazil: Implications for vertical fluid flow on continental margins. *J. Geophys. Res.*, 116:
648 B08103.

649 Gong, Z.S., Jin, Q., Qiu, Z., Wang, S., Meng, J., 1989. Geology, tectonics and evolution of the Pearl River Mouth
650 Basin. In: Zhu, X. (Ed.), *Chinese Sedimentary Basins*. Elsevier, Amsterdam, pp. 181-196.

651 Gong, Z.S., Li, S.T. 1997. *Continental Margin Basin Analysis and Hydrocarbon Accumulation of the Northern*
652 *South China Sea*. Science Press, Beijing, pp. 193-256.

653 Hall, R., 2002. Cenozoic geological and plate tectonic evolution of SE Asia and the SW Pacific: computer-based

654 reconstructions model and animations. *J. Asian Earth Sci.*, 20: 354-431.

655 Hampton, M.A., Lee, H.J., Locat, J., 1996. Submarine landslides. *Rev. Geophys.*, 34: 33-59.

656 He, Y., Zhong, G.F., Wang, L.L., Kuang, Z.G., 2014. Characteristics and occurrence of submarine
657 canyon-associated landslides in the middle of the northern continental slope, South China Sea. *Mar. Pet. Geol.*,
658 57: 546-560.

659 Jackson, C.A.L., 2012. The initiation of submarine slope failure and the emplacement of mass transport complexes
660 in salt-related minibasins: A three-dimensional seismic-reflection case study from the Santos Basin, offshore
661 Brazil. *GSA Bull.*, 124: 746-761.

662 Joanne, C., Collot, J.Y., Lamarche, G., Migeon, S., 2010. Continental slope reconstruction after a giant mass
663 failure, the example of the Matakaoa Margin, New Zealand. *Mar. Geol.*, 268: 67-84.

664 Judd, A.G., Hovland, M., 2007. *Seabed Fluid Flow: The Impact on Geology, Biology and the Marine Environment*.
665 Cambridge University Press, Cambridge, pp. 163-178.

666 Laberg, J.S., Vorren, T.O., Mienert, J., Haflidason, H., Bryn, P., Lien, R., 2003. Preconditions leading to the
667 Holocene Trænadjupet Slide offshore Norway. In: Locat, J., Mienert, J. (Eds.), *Advances in Natural and*
668 *Technological Hazards Research*. Kluwer, Dordrecht, The Netherlands, pp. 247- 254.

669 Lamarche, G., Joanne, C., Collot, J.Y., 2008. Successive, large mass-transport deposits in the south Kermadec
670 fore-arc basin, New Zealand: The Matakaoa Submarine Instability Complex. *Geochem. Geophys. Geosyst.*, 9:
671 Q04001.

672 Li, W., Wu, S.G., Völker, D., Zhao, F., Mi, L.J., Kopf, A., 2014b. Morphology, seismic characterization and
673 sediment dynamics of the Baiyun Slide Complex on the northern South China Sea margin. *J. Geol. Soc.*,
674 London, 171: 865-877.

675 Liu, B.J., Pang, X., Yan, C.Z., Liu, J., Lian, S.Y., He, M., Shen, J., 2011. Evolution of the Oligocene-Miocene shelf

676 slope-break zone in the Baiyun deep-water area of the Pearl River Mouth Basin and its significance in oil-gas
677 exploration. *Acta Pet. Sin.* 32: 234-242 (in Chinese with English abstract).

678 Løseth, H., Gading, M., Wensaas, L., 2009. Hydrocarbon leakage interpreted on seismic data. *Mar. Pet. Geol.*, 26:
679 1304-1309.

680 Lüdmann, T., Wong, H.K., 1999. Neotectonic regime on the passive continental margin of the northern South
681 China Sea. *Tectonophysics*, 311: 113-138.

682 Lüdmann, T., Wong, H.K., Wang, P., 2001. Plio-Quaternary sedimentation processes and neotectonics of the
683 northern continental margin of the South China Sea. *Mar. Geol.*, 172: 331-356.

684 Martel, S.J., 2004. Mechanics of landslide initiation as a shear fracture phenomenon. *Mar. Geol.*, 203: 319-339.

685 Maslin, M., Vilela, C., Mikkelsen, N., Grootes, P., 2005. Causes of catastrophic sediment failures of the Amazon
686 Fan. *Quat. Sci. Rev.*, 24: 2180-2193.

687 Masson, D.G., Harbitz, C.B., Wynn, R.B., Pedersen, G., Lovholt, F., 2006. Submarine landslides: processes,
688 triggers and hazard prediction. *Philosophical Transactions Series A: Mathematical, Physical, and Engineering*
689 *Sciences*, 364: 2009-2039.

690 Masson, D.G., Watts, A.B., Gee, M.J.R., Urgeles, R., Mitchell, N.C., Le Bas, T.P., Canals, M., 2002. Slope failures
691 on the flanks of the western Canary Islands. *Earth-Sci. Rev.*, 57: 1-35.

692 Moscardelli, L., Wood, L., Mann, P., 2006. Mass-transport complexes and associated processes in the offshore area
693 of Trinidad and Venezuela. *AAPG Bull.*, 90:1059-1088.

694 Nardin, T. R., Hein, F.J., Gorsline, D.S., Edwards, B.D., 1979. A review of mass movements processes, sediment
695 and acoustic characteristics, and contrasts in slope and baseof- slope systems versus canyon-fan-basin floor
696 system, in *Geology of Continental Slopes*, edited by L. J. Doyle and O. H. Pilkey Jr., Spec. Publ. Soc. Econ.
697 *Paleontol. Mineral.*, 27, 67-73.

698 CSI (China Seismic Information), 2017. (Accessed December 2017 from:
699 <http://www.csi.ac.cn/publish/main/813/4/index.html>).

700 Obelcz, J., Xu, K.H, Georgiou, I.Y., Maloney, J., Bentley, S.J., Miner, M.D., 2017. Sub-decadal submarine
701 landslides are important drivers of deltaic sediment flux: Insights from the Mississippi River Delta Front.
702 Geology, in press.

703 Omeru, T., Cartwright, J., 2015. Multistage, progressive slope failure in the Pleistocene pro-deltaic slope of the
704 West Nile Delta (Eastern Mediterranean). *Mar. Geol.*, 362: 76-92

705 Owen, M., Day, S., Maslin, M., 2007. Late Pleistocene submarine mass movements: occurrence and causes. *Quat.*
706 *Sci. Rev.*, 26: 958-978.

707 Pang, X., Chen, C.M., Peng, D.J., Zhou, D., Shao, L., He, M., Liu, B.J., 2008. Basic geology of Baiyun deep-water
708 area in the northern South China Sea. *China Offshore Oil and Gas*, 20: 216-222 (in Chinese with English
709 abstract).

710 Piper, D.J.W., Farre, J.A., Shor, A., 1985. Late Quaternary slumps and debris flows on the Scotian Slope. *Geol.*
711 *Soc. Am. Bull.*, 96: 1508-1517.

712 Piper, D.J.W., Pirmez, C., Manley, P.L., Long, D., Flood, R.D., Normark, W.R., Showers, W., 1997. Mass-transport
713 Deposits of the Amazon Fan, in R.D. Flood, D.J.W. Piper, A. Klaus, and L.C. Peterson (eds.), *Proceedings of*
714 *the Ocean Drilling Program, Scientific Results*, 155: 109-146.

715 Pope, E.L., Tailling, P.J., Carter, L., 2017. Which earthquakes trigger damaging submarine mass movements:
716 Insights from a global record of submarine cable breaks? *Mar. Geol.*, in press.

717 Posamentier, H.W., Kolla, V., 2003. Seismic geomorphology and stratigraphy of depositional elements in
718 deep-water settings. *J. Sediment Res.*, 73:367-388.

719 Ru, K., Pigott, J.D., 1986. Episodic rifting and subsidence in the South China Sea. *AAPG Bull.*, 70: 1136-1155.

720 Sawyer, D.E., Flemings, P.B., Dugan, B., Germaine, J.T., 2009. Retrogressive failures recorded in mass transport
721 deposits in the Ursa Basin, Northern Gulf of Mexico. *J. Geophys. Res.*, 114: B10102.

722 Sibuet, J.C., Yeh, Y.C., Lee, C.S., 2016. Geodynamics of the South China Sea. *Tectonophysics*, 692: 98-119.

723 Strasser, M., Moore, G.F., Kimura, G., Kopf, A.J., Underwood, M.B., Guo, J.H., Screaton, E.J., 2011. Slumping
724 and mass transport deposition in the Nankai fore arc: evidence from IODP drilling and 3-D reflection seismic
725 data. *Geochem. Geophys. Geosystems*, 12: Q0AD13.

726 Sultan, N., Cochonat, P., Canals, M., Cattaneo, A., Dennielou, B., Haflidason, H., Laberg, J., Long, D., Mienert, J.,
727 Trincardi, F., 2004. Triggering mechanisms of slope instability processes and sediment failures on continental
728 margins: a geotechnical approach. *Mar. Geol.*, 213: 291-321.

729 Sun, Q.L., Alves, T., Lu, X.Y., Chen, C.X., Xie, N.N. 2018. True volumes of slope failure estimated from a
730 Quaternary mass-transport deposit in the northern South China Sea. *Geophys. Res. Lett.*, in press.

731 Sun, Q.L., Alves, T., Xie, N.N., He, J.X., Li, W., Ni, X.L., 2017a. Free gas accumulations in basal shear zones of
732 mass-transport deposits (Pearl River Mouth Basin, South China Sea): An important geohazard on continental
733 slope basins. *Mar. Pet. Geol.*, 81: 17-32.

734 Sun, Q.L., Wu, S.G., Cartwright, J.A., Dong, D.D., 2012. Shallow gas and focused fluid flow systems in the Pearl
735 River Mouth Basin, northern South China Sea. *Mar. Geol.*, 315-318: 1-14.

736 Sun, Q.L., Wu, S.G., Cartwright, J.A., Wang, S.H., Lu, Y.T., Chen, D.X., Dong, D.D., 2014. Neogene igneous
737 intrusions in the northern South China Sea: Evidence from high-resolution three dimensional seismic data.
738 *Mar. Pet. Geol.*, 54: 83-95.

739 Sun, Q.L., Xie, X.N., Piper, D.J.W., Wu, J., Wu, S.G., 2017b. Three dimensional seismic anatomy of multi-stage
740 mass transport deposits in the Pearl River Mouth Basin, northern South China Sea: Their ages and kinematics.
741 *Mar. Geol.*, 393: 93-108.

- 742 Sun, Y.B., Wu, S.G., Wang, Z.J., Li, Q.P., Wang, X.J., Dong, D.D., Liu, F., 2008. The geometry and deformation
743 characteristics of Baiyun Submarine Landslide. *Marine Geology & Quaternary Geology*, 28: 70-77 (in
744 Chinese with English abstract).
- 745 Sun, Z., Zhou, D., Pang, X., Huang, C.J., Chen, C.M., Zhong, Z.H., He, M., Xu, H.H., 2008. Dynamics analysis of
746 the Baiyun Sag in the Pearl River Mouth basin, North of South China Sea. *Acta Geol. Sin.* 82 (1): 73-83 (in
747 Chinese with English abstract).
- 748 Taylor, B., Hayes, D.E., 1983. Origin and history of the South China Sea basin, in the tectonic and geologic
749 evolution of Southeast Asian seas and islands: part 2. In: Hayes, D.E. (Ed.), *Geophysical Monograph Series*,
750 vol. 27. AGU, Washington, D. C., pp. 23-56.
- 751 Tripsanas, E.K., Piper, D.J.W., Jenner, K.A., Bryant, W.R., 2008. Submarine mass-transport facies: new
752 perspectives on flow processes from cores on the eastern North American margin. *Sedimentology*, 55: 97-136.
- 753 Wang, L., Wu, S.G., Li, Q.P., Wang, D.W., Fu, S.Y., 2014. Architecture and development of a multi-stage Baiyun
754 submarine slide complex in the Pearl River Mouth Canyon, northern South China Sea. *Geo-Mar. Lett.*, 34:
755 327-343.
- 756 Wang, P., Prell, W.L., Blum, P., et al. (Eds.), 2000. *Proc. ODP, Init. Rept. 184 [CD-ROM]*. Ocean Drilling Program,
757 Texas A & M University, College Station TX 77845-9547, USA .
- 758 Wang, X.X., Wang, Y.M., He, M., Chen, W.T., Zhuo, H.T., Gao, S.M., Wang, M.H., Zhou, J.W., 2017. Genesis and
759 evolution of the mass transport deposits in the middle segment of the Pearl River canyon, South China Sea:
760 Insights from 3D seismic data. *Mar. Pet. Geol.*, 88: 555-574.
- 761 Wright, S.G., Rathje, E.M., 2003. Triggering mechanisms of slope instability and their relationship to Earthquakes
762 and Tsunamis. *Pure Appl. Geophys.*, 160: 1865-1877.
- 763 Wu, S.G., Wang, D.W., Yao, G.S., 2015. Geophysical recognition of deep-water deposition and reservoir in the

- 764 South China Sea. Science Press, Beijing, pp. 25-231.
- 765 Xie, H., Zhou, D., Li, Y.P., Pang, X., Li, P.C., Chen, G.H., Li, F.C., Cao, J.H., 2014. Cenozoic tectonic subsidence
766 in deepwater sags in the Pearl River Mouth Basin, northern South China Sea. *Tectonophysics*, 615-616:
767 182-198.
- 768 Xie, H., Zhou, D., Pang, X., Li, Y.P., Wu, X.J., Qiu, N., Li, P.C., Chen, G.H., 2013. Cenozoic sedimentary
769 evolution of deepwater sags in the Pearl River Mouth Basin, northern South China Sea. *Mar. Geophys. Res.*
770 34: 159-173.
- 771 Xie, X.N., Mülle, R.D., Li, S.T., Gong, Z.S., Steinberger, B., 2006. Origin of anomalous subsidence along the
772 Northern South China Sea margin and its relationship to dynamic topography. *Mar. Petrol. Geol.*, 23:
773 745-765.
- 774 Xu, S., Yang, S., Huang, L., 1995. The application of sequence stratigraphy to stratigraphic correlation. *Earth Sci.*
775 *Front.*, 2: 115-123.
- 776 Yan, P., Di, D., Liu, Z.S., 2001. A crustal structure profile across the northern continental margin of the South
777 China Sea. *Tectonophysics*, 338: 1-21.
- 778 Yu, H.S., 1994. Structure, stratigraphy and basin subsidence of Tertiary basins along the Chinese southeastern
779 continental margin. *Tectonophysics*, 253: 63-76.
- 780 Zhu, M.Z., Graham, S., Pang, X., McHargue, T., 2010. Characteristics of migrating canyons from the middle
781 Miocene to present: implications for paleoceanographic circulation, northern South China Sea. *Mar. Pet. Geol.*
782 27, 307-319.
- 783 Zhu, W., Huang, B., Mi, L., Wilkins, R.W., Fu, N., Xiao, X., 2009. Geochemistry, origin, and deep-water
784 exploration potential of natural gases in the Pearl River Mouth and Qiongdongnan Basins, South China Sea.
785 *AAPG Bull.*, 93: 741-761.

Figure captions

Figure 1: Geological setting and location of Pearl River Mouth Basin in the northern South China Sea. Inset (top left): regional setting. The location of MTDs is marked with white polygon. Locations of Fig. 3 (red dashed square) and Dongsha Islands (red circle) are labeled.

Figure 2: Schematic stratigraphic column of the Pearl River Mouth Basin (mainly modified from Pang et al. (2008)). The red lines in 'Tectonic Events' represent the main stages of each tectonic episode. This study is focused on the Quaternary strata (blue rectangle).

Figure 3: (a) Locations of 2-D seismic lines crossing ODP/IODP sites, 3-D seismic surveys and ODP/IODP sites used to sequence correlation. Main structures of Pearl River Mouth Basin and adjacent area since surface T_3 (middle Miocene) are superimposed on this map; (b) Main elements of seabed morphology and the structures observed within the shallow strata. The escarpment of the slope failures, canyons, seabed troughs and Central Valley, continent-ocean boundary (COB), axis of continent-ocean boundary (connected peaks of COB) and the neck of COB can be marked.

Figure 4: (a) 3-D seismic profile crosses through the migrating canyon zone. The canyons with complex internal seismic reflections migrated upward and eastward since middle Miocene (surface T_3); (b) 3-D seismic profile crosses through northern scarp of the MTDs. Free gas which has stacked high-amplitude seismic anomalies occurs around the scarp of MTDs within the strata from middle Miocene to recent; (c) 2-D seismic profile crosses through burial igneous complex in

the lower slope. Normal faults and stacked free gas occur within the overlying folded strata and onlap seismic reflections are observed in the northeastern flank of this structure. MTDs with chaotic/blanking seismic reflections, coarse-grained sediments with high-amplitude seismic reflections, polygonal faults and Central Valley (sediment fairway) are labeled; (d) 2-D seismic profile crosses through a large igneous complex in the middle slope. The igneous complex deforms thick strata, even towards to the seabed. Coarse-grained sediments, free gas, MTDs, escarpment and possible gas hydrate are labeled. See locations in [Fig. 3a](#).

Figure 5: (a) Three slope failure events which separated by strong negative seismic reflections are identified in the 3-D seismic profile. The ages of seismic reflections/MTDs are adopted from [Sun et al., \(2017b\)](#); (b) Age-depth model and estimated sedimentation rate for IODP Site U1432, based on biostratigraphic and paleomagnetic datums (modified from [Expedition 349 Scientists \(2014\)](#)); (c) A 2-D seismic profile in the slope of PRMB crosscuts all the four failure events. The gas-charged coarse-grained sediments, Central Valley (sediment fairway), free gas, igneous complex and MTDs are labeled; (d) A 2-D seismic profile crosscuts the ocean basin, continent-ocean boundary (COB) and two MTDs (MTDo1 and MTDo2). The lower part of COB comprises igneous complexes and its upper part is composed of depositional strata. See locations in [Fig. 3a](#).

Figure 6: (a) Thicknesses of MTDa on the slope and MTDo1 in the ocean basin are superimposed on the shaded map. The depocenters of MTDa are along the Central Valley (brown polygon); (b) and (c) 3-D visualization maps of two small-scale evacuation zones which are supposed as the

probable source areas for MTDa and MTD_{o1}; (d) A NW-SE 2-D seismic profile shows MTD_b is strongly eroded; (e) A NW-SE 2-D seismic profile crosscuts the eastern part of MTDa which wedges out to the downslope; (f) A SW-NE 2-D seismic profile immediately located outside the neck of COB. Sediments onlap onto the flanks of COB started from middle Miocene (surface T₃).

Figure 7: (a) Thicknesses of MTD_b on the slope and MTD_{o2} in the ocean basin are superimposed on the shaded map. The locations of (b) - (f) are labeled; (b) Flattening variance slice of the base of MTD_b in its head zone. Linear structures (erosive grooves), scarps (red dashed line), faults (pink lines) and induced flow directions (purple dashed arrows) are labeled; (c) A 3-D seismic profile shows the lateral scarp of MTD_b is bounded by normal faults. Free gas (negative seismic reflection anomalies) is also observed; (d) A 3-D seismic profile crosses through the headscarp of MTD_b, showing steep headscarp and chaotic/blanking seismic characteristics of MTD_b. There are not representative extensional structures in the head zone; (e) A 2-D seismic profile in the middle slope shows the superimposed relationship of MTD_b and MTD_c. Large-scale lateral scarps are identified in both sides of the depressions. Seismic reflections onlapping onto the surface T₂, free gas, gas chimney and igneous complexes are marked; (f) A NW-SE 2-D seismic profile mainly located in the lower slope shows the high-amplitude seismic reflections (coarse-grained sediments) onlap toward both the upslope and COB, and they become thinner towards to the upslope. Weak seismic reflections (fine-grained sediments) directly overlaying the coarse-grained sediments are also observed; (g) Enlargement of part of (b) clearly demonstrates the linear structures in the variance slice.

Figure 8: (a) Residual thickness of MTDC is superimposed on the shaded map. Three depocenters, two against the lateral scarps and one just at the shadow of the igneous complexes (red dashed ellipse), are observed; Part of its western boundary is lineated by the Central Valley (pink polygon); (b) Flattening variance slice of the base of MTDC (modified from [Sun et al. \(2017b\)](#)). Linear structures indicate the failed sediments mainly flowing from the NW to SE (red dashed arrows). Arcuate scarps (Scarp 1 - 5) and tilted blocks are marked; (c) Slope dip change (cyan dashed line in (a)) is observed in the upper part of MTDC and it is interpreted as the headscarp; (d) A NW-SE 2-D seismic profile crosses through the head zone of MTDC. Large igneous complexes are located immediately against the MTDC. High-amplitude seismic reflections (coarse-grained sediments) wedge out towards to the upslope.

Figure 9: (a) Residual thickness of MTDD superimposed on the shaded map. The locations of (b) - (e) are labeled; (b) - (c): Vertical profiles show the slope dip changes where the headscarp of MTDD is probably located (red dashed line in (a)); (d) A NW-SE 2-D seismic profile shows the relationships between MTDs (MTDa, MTDb and MTDD), coarse-grained sediments, fine-grained sediments. Onlap seismic reflections and gas-charged coarse sediments are also observed; (e) A NW-SE 2-D seismic profile shows the superimposed relationships of four MTDs. High-amplitude/weak seismic reflections (coarse/fine-grained sediments), lateral scarps, seamount, onlap seismic reflections, polygonal faults and seismic reflection surfaces are labeled.

Figure 10: Schematic summaries showing susceptible factors (preconditions) of seal-level change ([Xu et al., 1995](#)), sedimentation rates (Deep-water area of PRMB from [Xie et al. \(2013\)](#), ODP Site

1146 from Wang et al. (2000) and IODP Site U1432 from Expedition 349 Scientists. (2014)),
subsidence/uplifting (Xie et al., 2014), canyon activity (Zhu et al., 2010), lithology (Deep-water
area of PRMB deduced from this study, ODP Site 1146 from Wang et al. (2000) and IODP Site
U1432 from Expedition 349 Scientists. (2014)) and free gas accumulations (Free gas in the lower
part of canyon zone from Sun et al. (2012), free gas around the eastern scarp from Sun et al.
(2017a) and free gas in the coarse-grained sediments deduced from this study), igneous activities
(Lüdmann and Wong, 1999; Sun et al., 2014; Fan et al., 2017) and possible trigger factor
(earthquake) for the slope failures in the study area. Their contributions for the occurrences of
slope failures are estimated.

Figure 11: Occurrences of the failure plane and weak layer of slope failure. Transition zone of
fine/coarse-grained sediments forms the weak layer. The fluids from underlying strata charge into
the coarse-grained sediments and migrate towards to the upslope. The normal faults and
overpressure resulting from fluid accumulation and thinning of coarse-grained strata are probably
responsible for the slope break which usually occurs at the flanks of underlying igneous
complexes or basement highs.

Figure 12: Formation processes of the repeated slope failures from middle Miocene to the end of
emplacement of MTDa. (a) Stage I: In the early middle Miocene, a large long negative relief
(depression) surrounded by topographic highs (massifs) had already formed; (b) Stage II: From
early middle Miocene to early Pleistocene (beginning of MTDd), turbidites transported via the
slope canyons deposited on the slope from lower slope to middle slope. Coarse-grained sediments

896 and fine-grained sediments were dominated in the early and late stages, respectively; (c) Stage III:
897 Possibly triggered by earthquakes, MTDd formed in the lower slope; (d) Stage IV: MTDc
898 emplaced in the middle-lower slope and eroded part of MTDd; (e) Stage V: Catastrophic MTDb
899 involved the whole depression and evacuated most parts of the slope (only two main depositional
900 zones could be observed); (f) Stage VI: Small-scale MTDa were probably sourced from two slope
901 failure areas in the lower slope. Please see text for details.
902

Figure 1

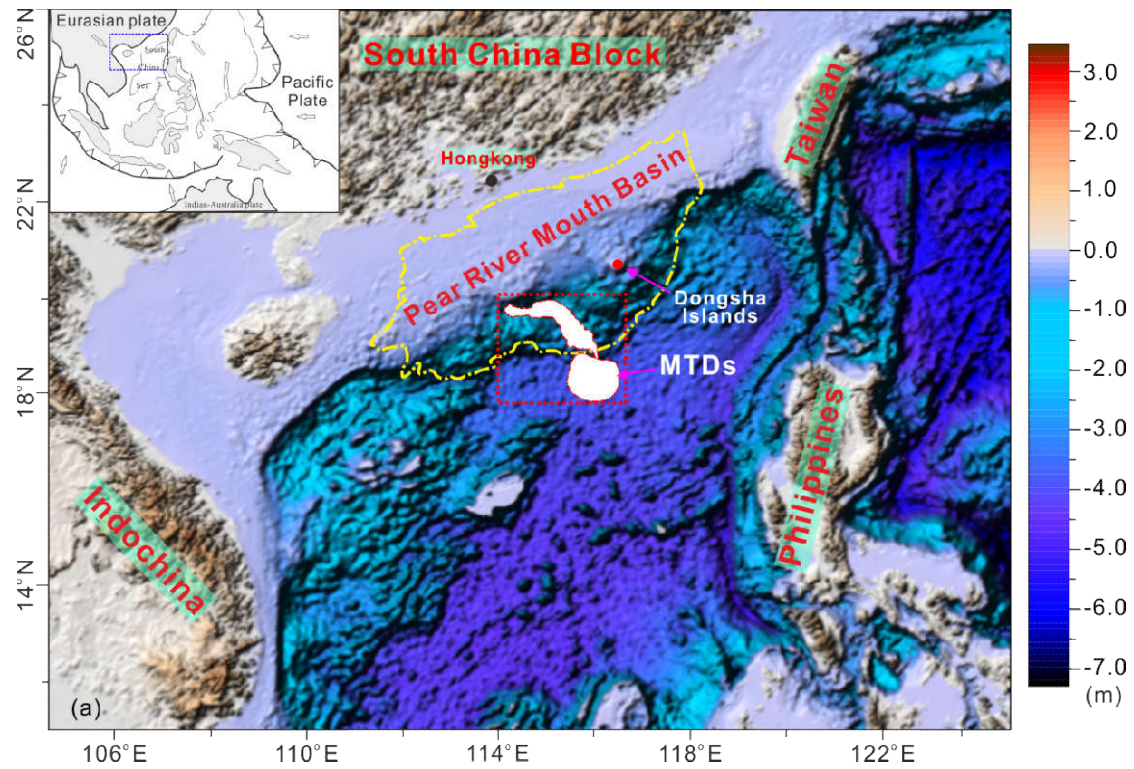
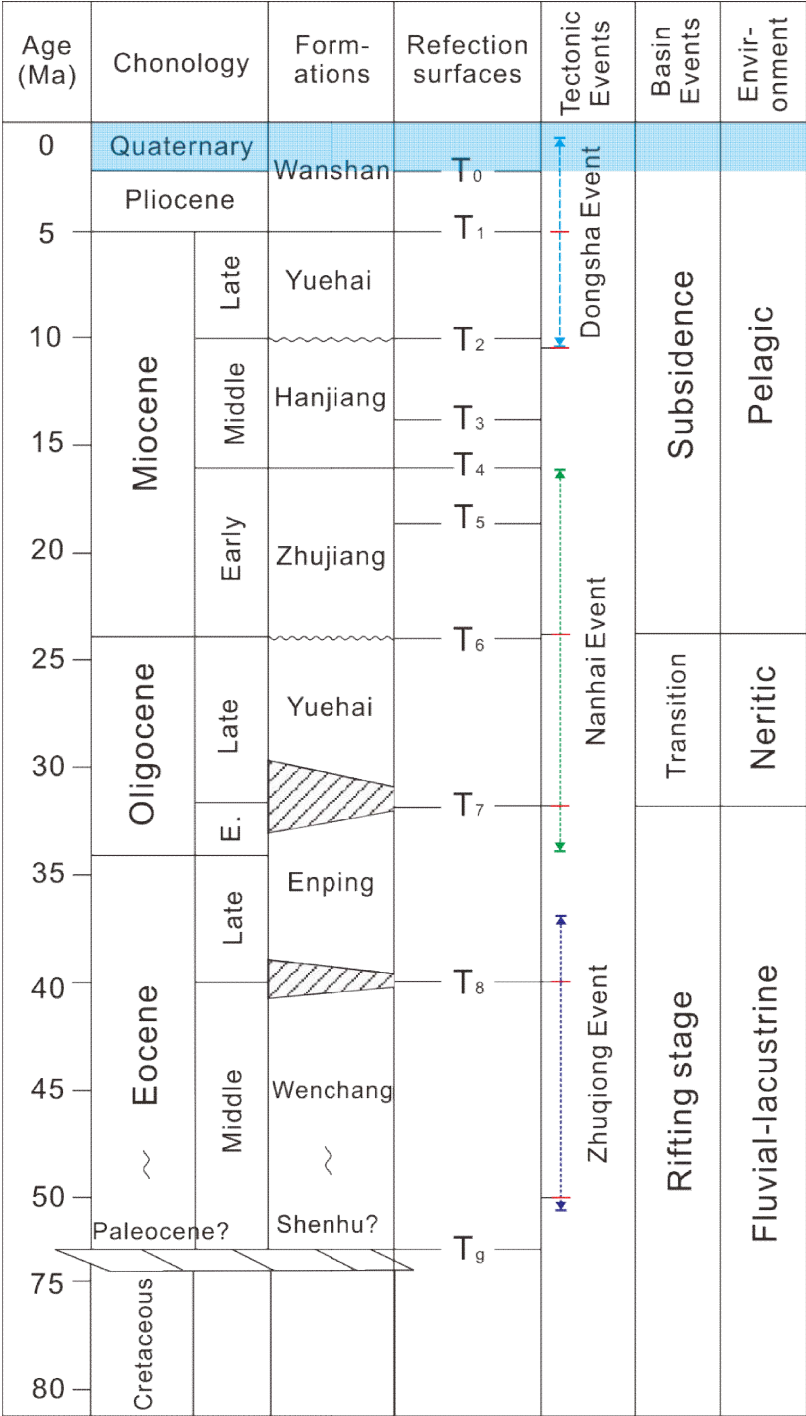


Figure 1: Geological setting and location of Pearl River Mouth Basin in the northern South China Sea. Inset (top left): regional setting. The location of MTDs is marked with white polygon. Locations of Fig. 3 (red dashed square) and Dongsha Islands (red circle) are labeled.

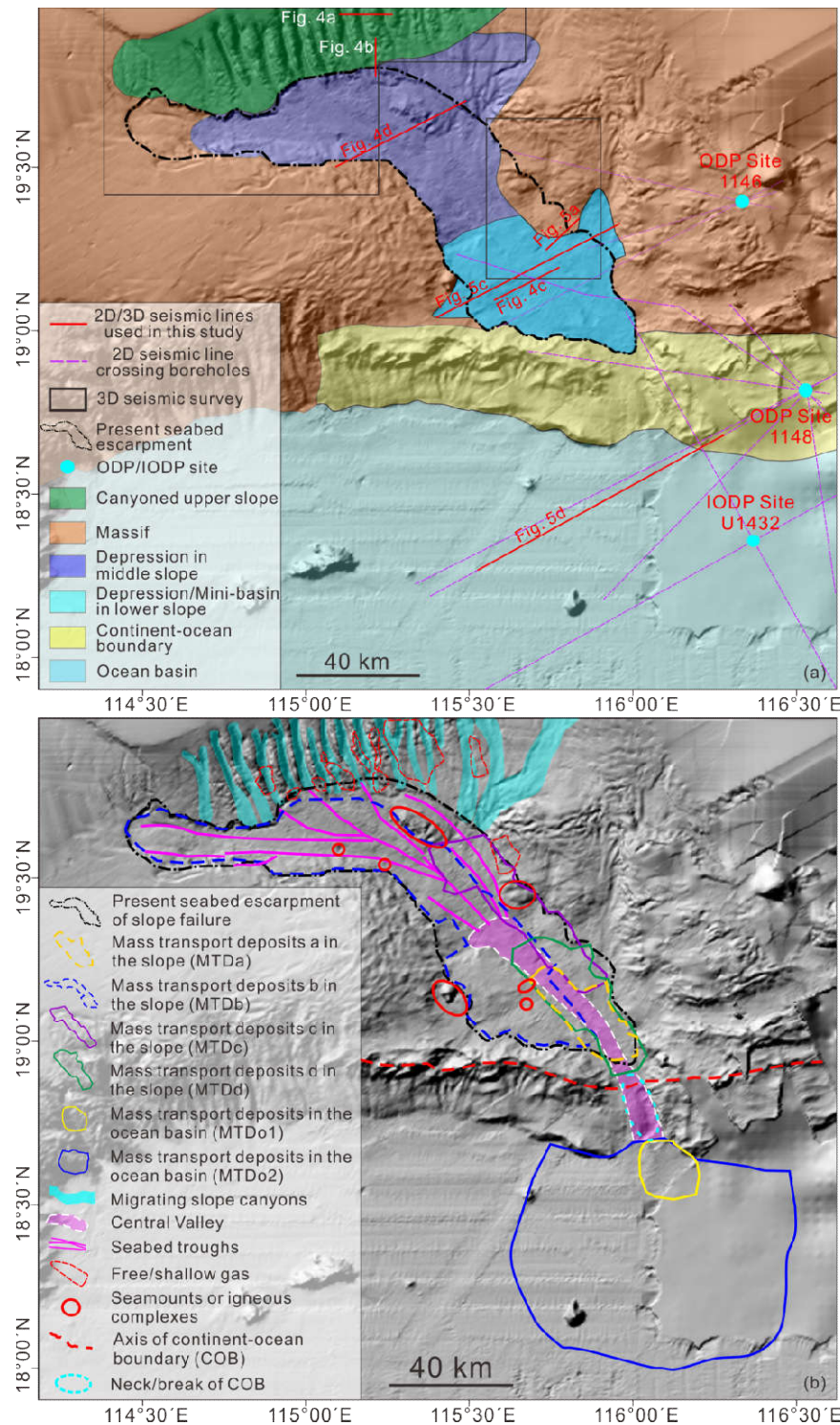
910 Figure 2



911

912 Figure 2: Schematic stratigraphic column of the Pearl River Mouth Basin (mainly modified from
913 Pang et al. (2008)). The red lines in 'Tectonic Events' represent the main stages of each tectonic
914 episode. This study is focused on the Quaternary strata (blue rectangle).

915



917
918 Figure 3: (a) Locations of 2-D seismic lines crossing ODP/IODP sites, 3-D seismic surveys and
919 ODP/IODP sites used to sequence correlation. Main structures of Pearl River Mouth Basin and
920 adjacent area since surface T_3 (middle Miocene) are superimposed on this map; (b) Main elements
921 of seabed morphology and the structures observed within the shallow strata. The escarpment of
922 the slope failures, canyons, seabed troughs and Central Valley, continent-ocean boundary (COB),
923 axis of continent-ocean boundary (connected peaks of COB) and the neck of COB can be marked.

Figure 4

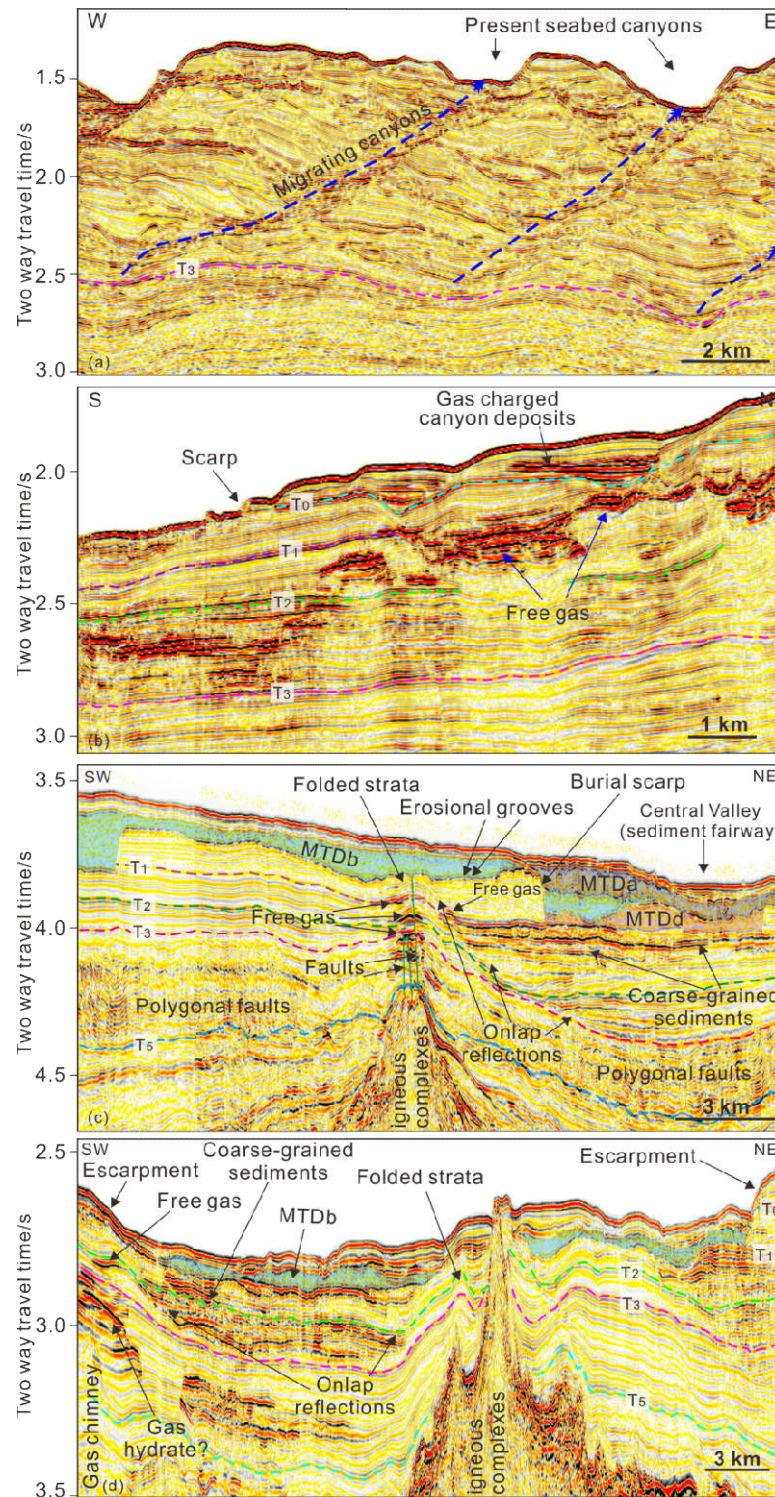


Figure 4: (a) 3-D seismic profile crosses through the migrating canyon zone. The canyons with complex internal seismic reflections migrated upward and eastward since middle Miocene (surface T₃); (b) 3-D seismic profile crosses through northern scarp of the MTDs. Free gas which has stacked high-amplitude seismic anomalies occurs around the scarp of MTDs within the strata from middle Miocene to recent; (c) 2-D seismic profile crosses through burial igneous complex in

the lower slope. Normal faults and stacked free gas occur within the overlying folded strata and onlap seismic reflections are observed in the northeastern flank of this structure. MTDs with chaotic/blanking seismic reflections, coarse-grained sediments with high-amplitude seismic reflections, polygonal faults and Central Valley (sediment fairway) are labeled; (d) 2-D seismic profile crosses through a large igneous complex in the middle slope. The igneous complex deforms thick strata, even towards to the seabed. Coarse-grained sediments, free gas, MTDs, escarpment and possible gas hydrate are labeled. See locations in [Fig. 3a](#).

Figure 5

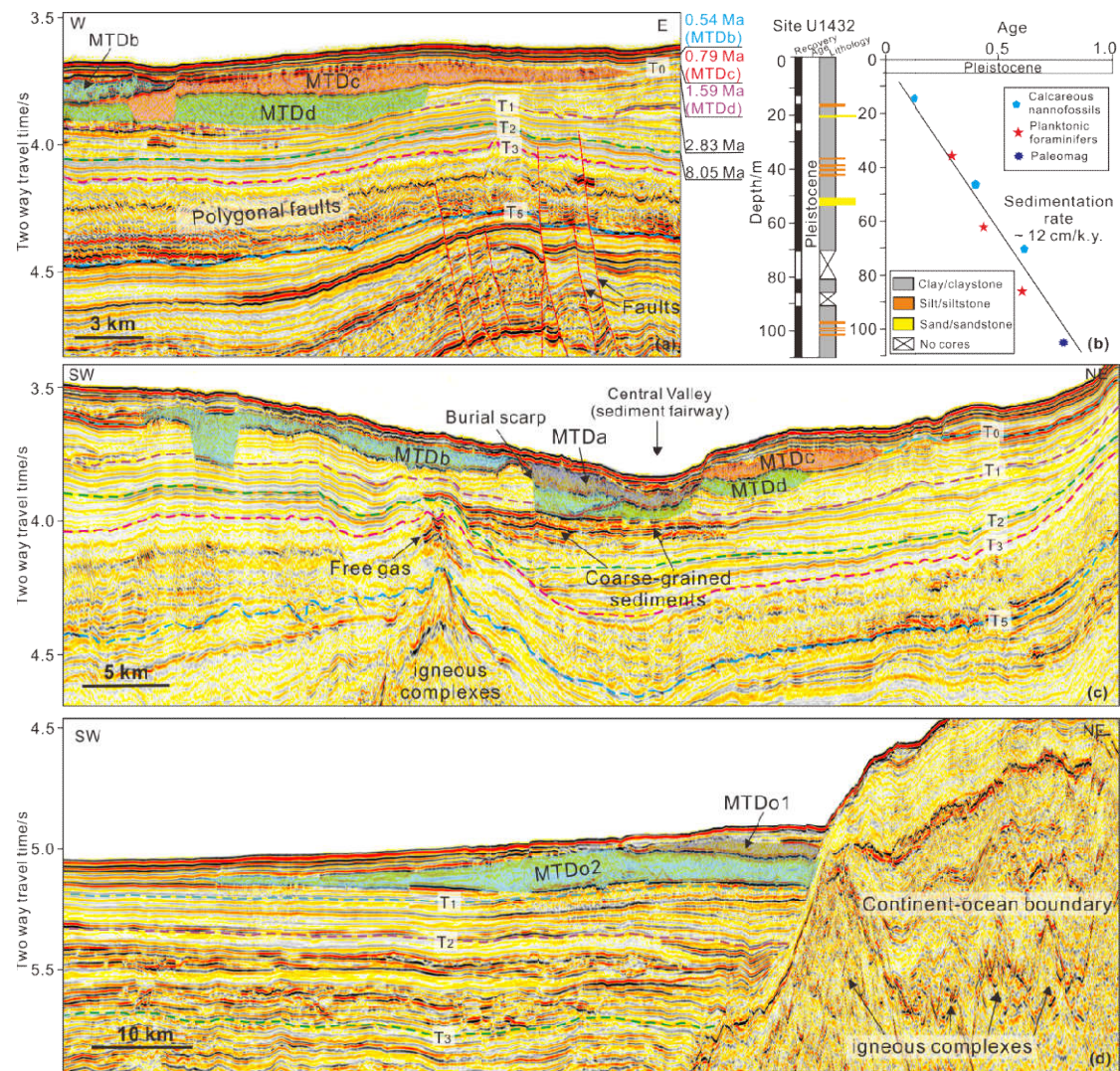
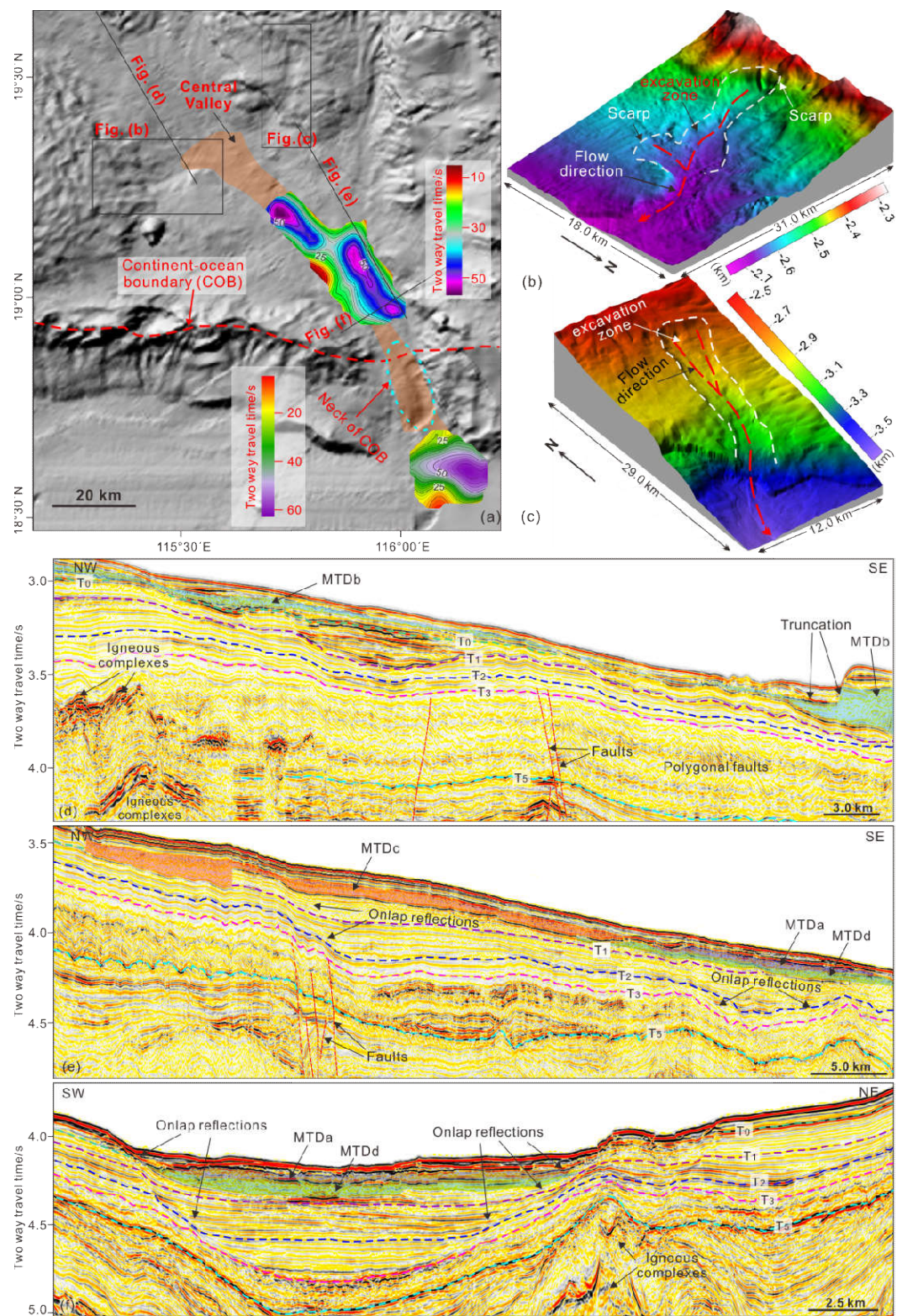
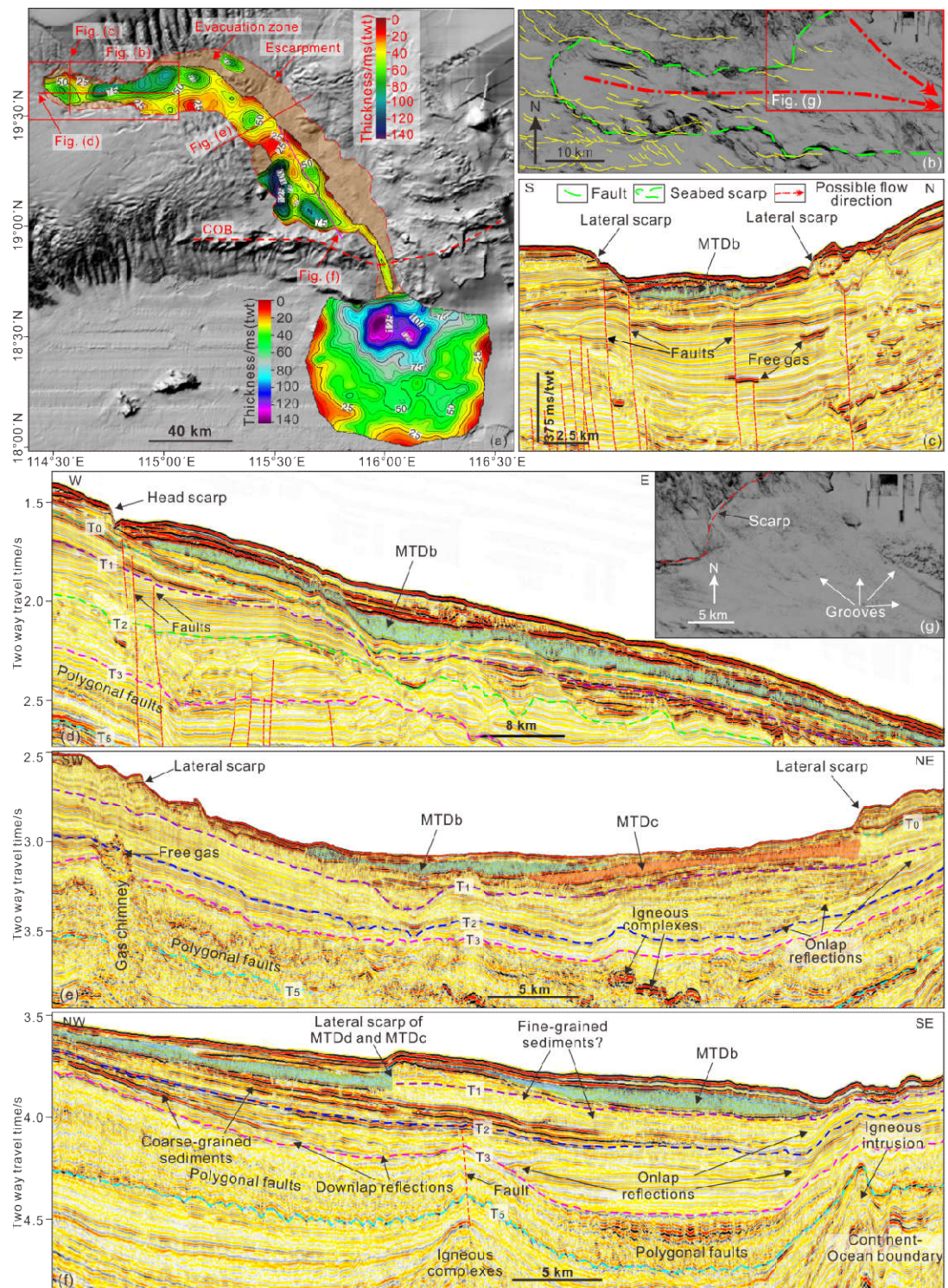


Figure 5: (a) Three slope failure events which separated by strong negative seismic reflections are identified in the 3-D seismic profile. The ages of seismic reflections/MTDs are adopted from Sun et al., (2017b); (b) Age-depth model and estimated sedimentation rate for IODP Site U1432, based on biostratigraphic and paleomagnetic datums (modified from Expedition 349 Scientists (2014)); (c) A 2-D seismic profile in the slope of PRMB crosscuts all the four failure events. The gas-charged coarse-grained sediments, Central Valley (sediment fairway), free gas, igneous complex and MTDs are labeled; (d) A 2-D seismic profile crosscuts the ocean basin, continent-ocean boundary (COB) and two MTDs (MTDo1 and MTDo2). The lower part of COB comprises igneous complexes and its upper part is composed of depositional strata. See locations in Fig. 3a.



954
955 Figure 6: (a) Thicknesses of MTDa on the slope and MTD01 in the ocean basin are superimposed
956 on the shaded map. The depocenters of MTDa are along the Central Valley (brown polygon); (b)
957 and (c) 3-D visualization maps of two small-scale evacuation zones which are supposed as the
958 probable source areas for MTDa and MTD01; (d) A NW-SE 2-D seismic profile shows MTDb is

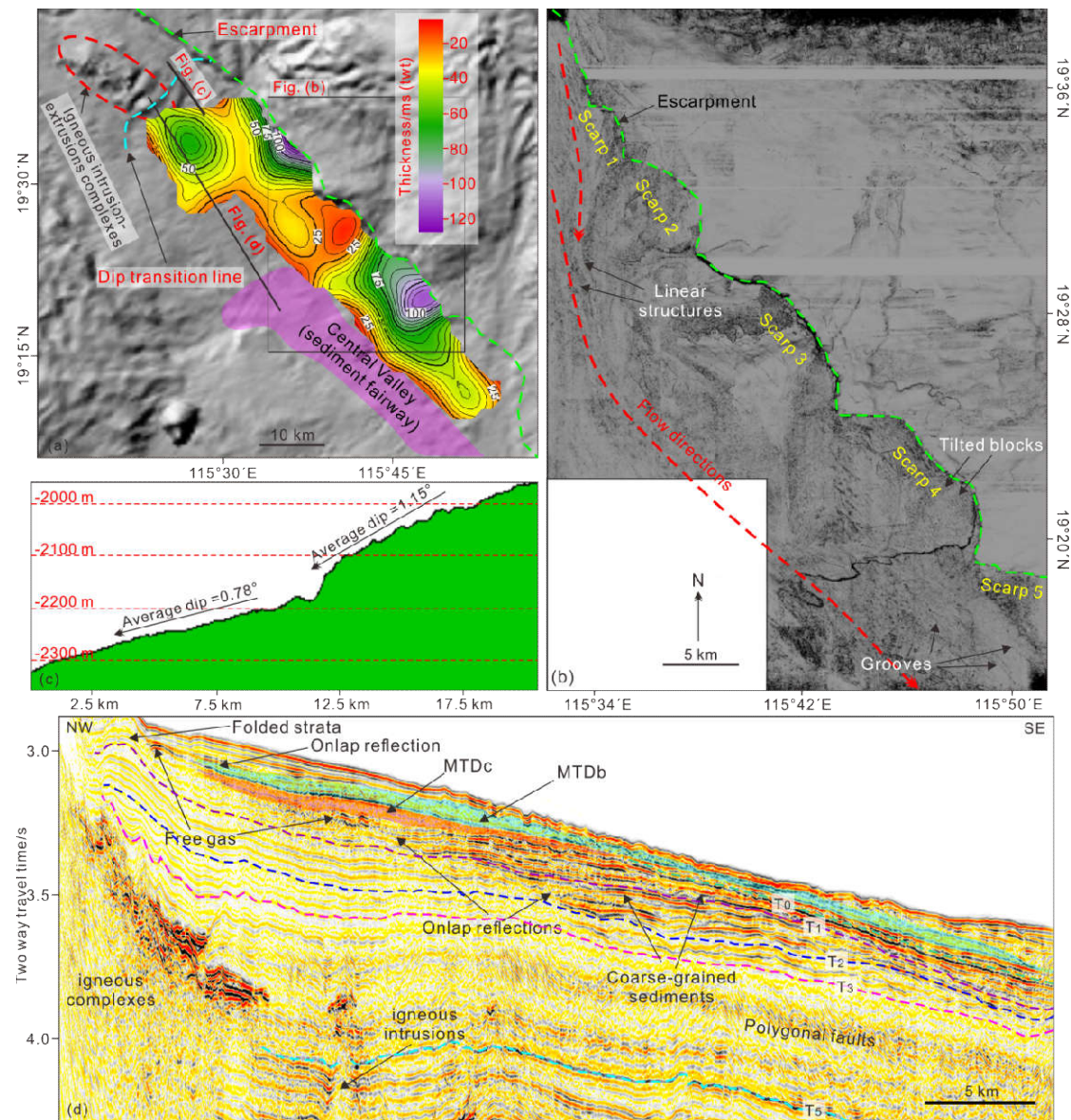
959 strongly eroded; (e) A NW-SE 2-D seismic profile crosscuts the eastern part of MTDa which
960 wedges out to the downslope; (f) A SW-NE 2-D seismic profile immediately located outside the
961 neck of COB. Sediments onlap onto the flanks of COB started from middle Miocene (surface T₃).
962



964
965 Figure 7: (a) Thicknesses of MTDb on the slope and MTD02 in the ocean basin are superimposed
966 on the shaded map. The locations of (b) - (f) are labeled; (b) Flattening variance slice of the base
967 of MTDb in its head zone. Linear structures (erosive grooves), scarp (red dashed line), faults
968 (pink lines) and induced flow directions (purple dashed arrows) are labeled; (c) A 3-D seismic
969 profile shows the lateral scarp of MTDb is bounded by normal faults. Free gas (negative seismic
970 reflection anomalies) is also observed; (d) A 3-D seismic profile crosses through the headscarp of

MTDb, showing steep headscarp and chaotic/blanking seismic characteristics of MTDb. There are not representative extensional structures in the head zone; (e) A 2-D seismic profile in the middle slope shows the superimposed relationship of MTDb and MTDc. Large-scale lateral scarps are identified in both sides of the depressions. Seismic reflections onlapping onto the surface T₂, free gas, gas chimney and igneous complexes are marked; (f) A NW-SE 2-D seismic profile mainly located in the lower slope shows the high-amplitude seismic reflections (coarse-grained sediments) onlap toward both the upslope and COB, and they become thinner towards to the upslope. Weak seismic reflections (fine-grained sediments) directly overlaying the coarse-grained sediments are also observed; (g) Enlargement of part of (b) clearly demonstrates the linear structures in the variance slice.

982 Figure 8



983
984 Figure 8: (a) Residual thickness of MTDc is superimposed on the shaded map. Three depocenters,
985 two against the lateral scarps and one just at the shadow of the igneous complexes (red dashed
986 ellipse), are observed; Part of its western boundary is lineated by the Central Valley (pink
987 polygon); (b) Flattening variance slice of the base of MTDc (modified from Sun et al. (2017b)).
988 Linear structures indicate the failed sediments mainly flowing from the NW to SE (red dashed
989 arrows). Arcuate scarps (Scarp 1 - 5) and tilted blocks are marked; (c) Slope dip change (cyan
990 dashed line in (a)) is observed in the upper part of MTDc and it is interpreted as the headscarp; (d)
991 A NW-SE 2-D seismic profile crosses through the head zone of MTDc. Large igneous complexes
992 are located immediately against the MTDc. High-amplitude seismic reflections (coarse-grained
993 sediments) wedge out towards to the upslope.
994

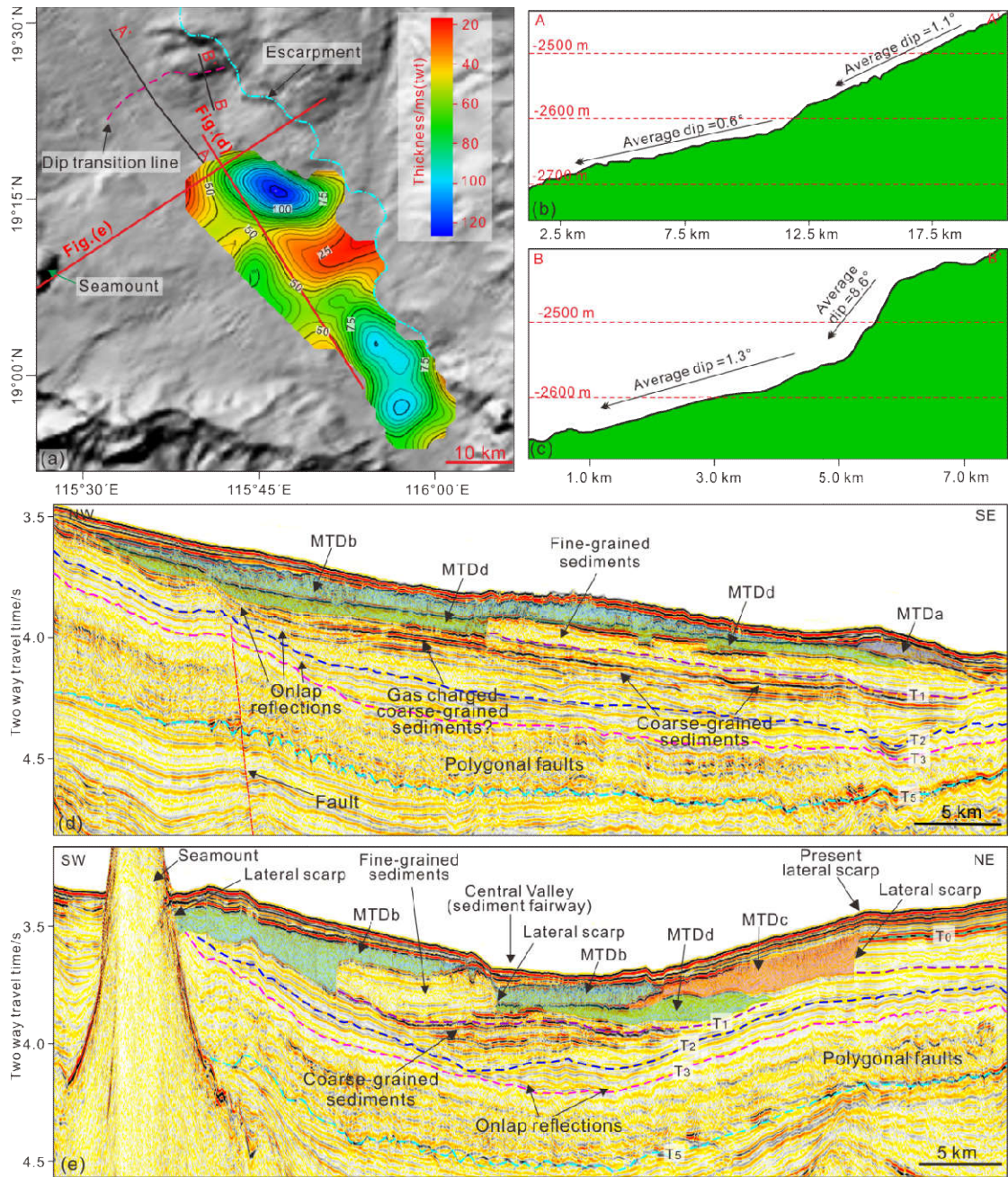
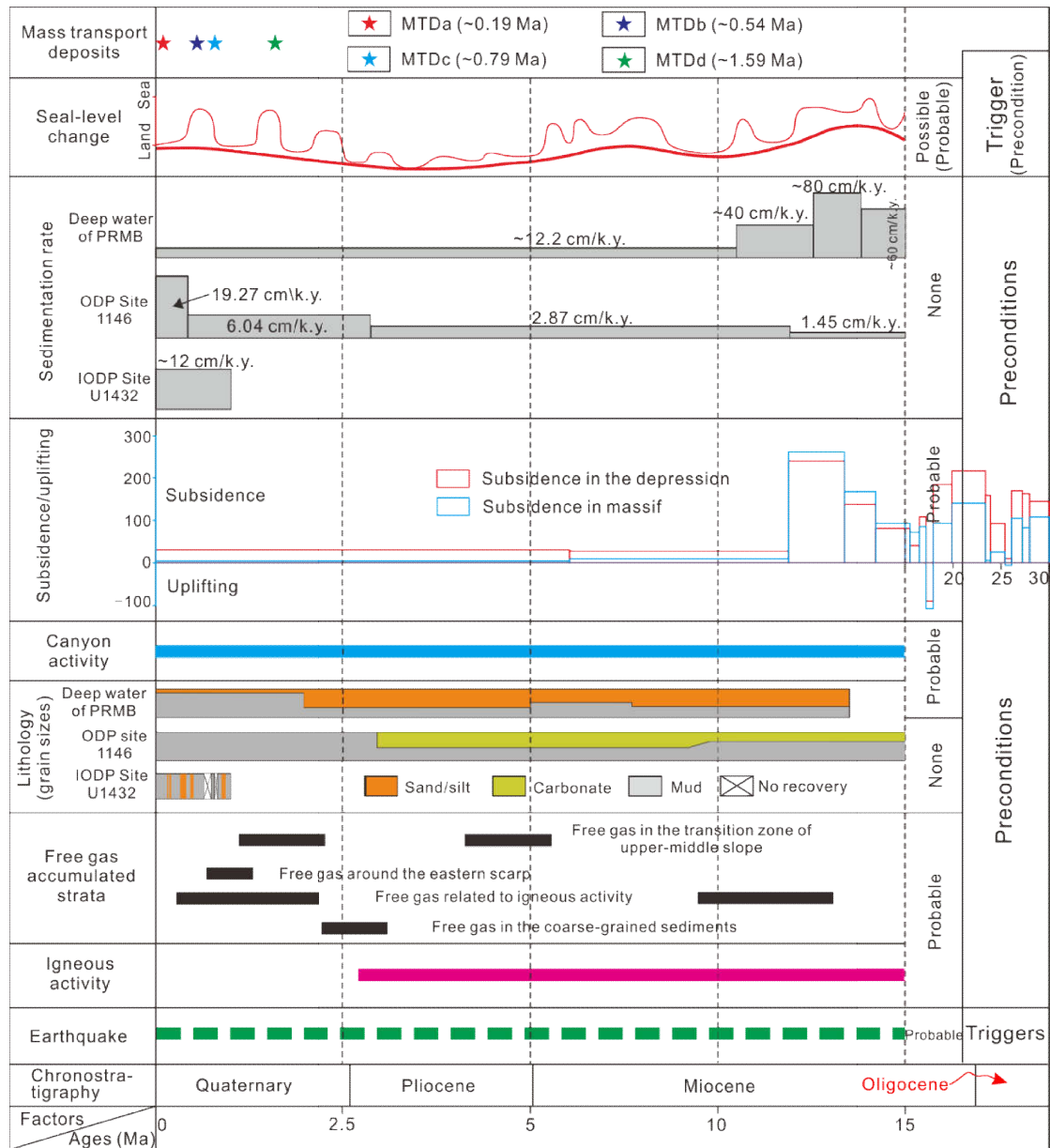


Figure 9: (a) Residual thickness of MTDD superimposed on the shaded map. The locations of (b) - (e) are labeled; (b) - (c): Vertical profiles show the slope dip changes where the headscarp of MTDD is probably located (red dashed line in (a)); (d) A NW-SE 2-D seismic profile shows the relationships between MTDs (MTDa, MTDb and MTDD), coarse-grained sediments, fine-grained sediments. Onlap seismic reflections and gas-charged coarse sediments are also observed; (e) A NW-SE 2-D seismic profile shows the superimposed relationships of four MTDs. High-amplitude/weak seismic reflections (coarse/fine-grained sediments), lateral scarps, seamount, onlap seismic reflections, polygonal faults and seismic reflection surfaces are labeled.

1006 Figure 10



1007
1008 Figure 10: Schematic summaries showing susceptible factors (preconditions) of seal-level change
1009 (Xu et al., 1995), sedimentation rates (Deep-water area of PRMB from Xie et al. (2013), ODP Site
1010 1146 from Wang et al. (2000) and IODP Site U1432 from Expedition 349 Scientists. (2014)),
1011 subsidence/uplifting (Xie et al., 2014), canyon activity (Zhu et al., 2010), lithology (Deep-water
1012 area of PRMB deduced from this study, ODP Site 1146 from Wang et al. (2000) and IODP Site
1013 U1432 from Expedition 349 Scientists. (2014)) and free gas accumulations (Free gas in the lower
1014 part of canyon zone from Sun et al. (2012), free gas around the eastern scarp from Sun et al.
1015 (2017a) and free gas in the coarse-grained sediments deduced from this study), igneous activities
1016 (Lüdmann and Wong, 1999; Sun et al., 2014; Fan et al., 2017) and possible trigger factor
1017 (earthquake) for the slope failures in the study area. Their contributions for the occurrences of
1018 slope failures are estimated.

Figure 11

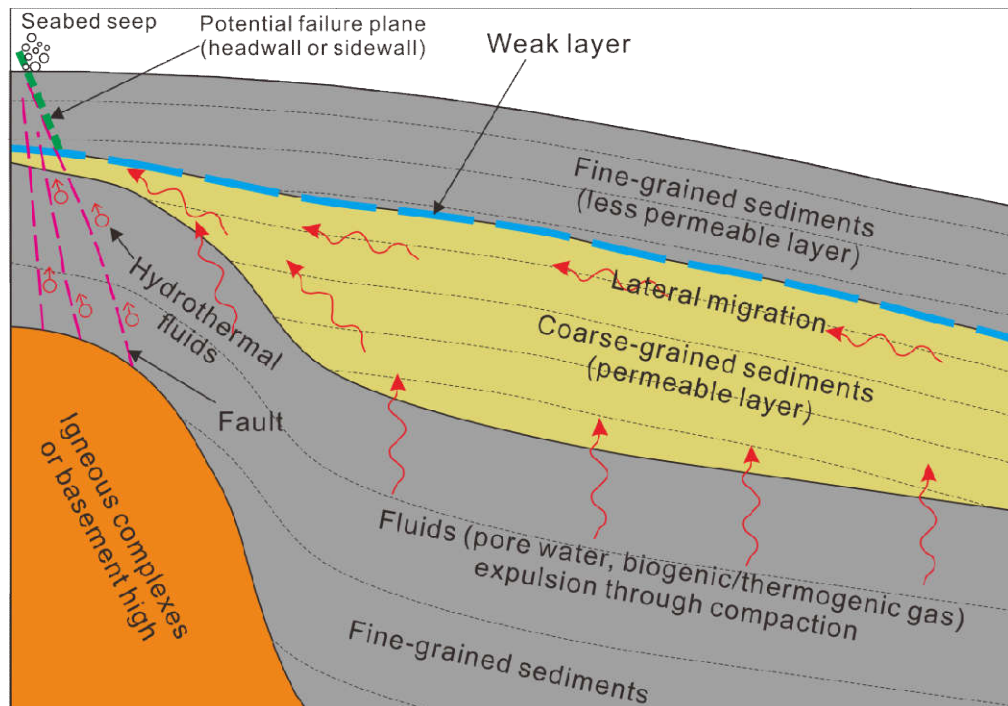
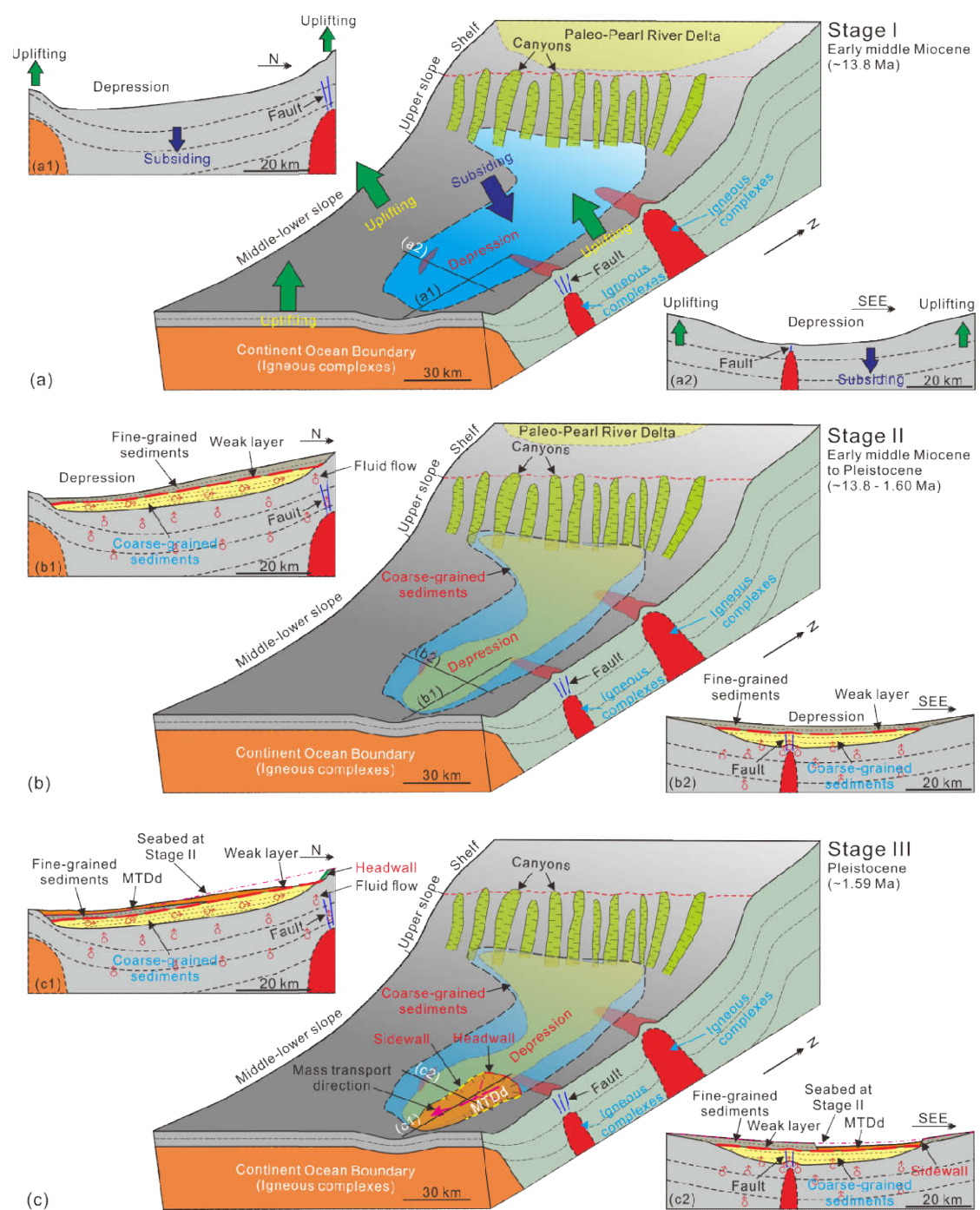


Figure 11: Occurrences of the failure plane and weak layer of slope failure. Transition zone of fine/coarse-grained sediments forms the weak layer. The fluids from underlying strata charge into the coarse-grained sediments and migrate towards to the upslope. The normal faults and overpressure resulting from fluid accumulation and thinning of coarse-grained strata are probably responsible for the slope break which usually occurs at the flanks of underlying igneous complexes or basement highs.

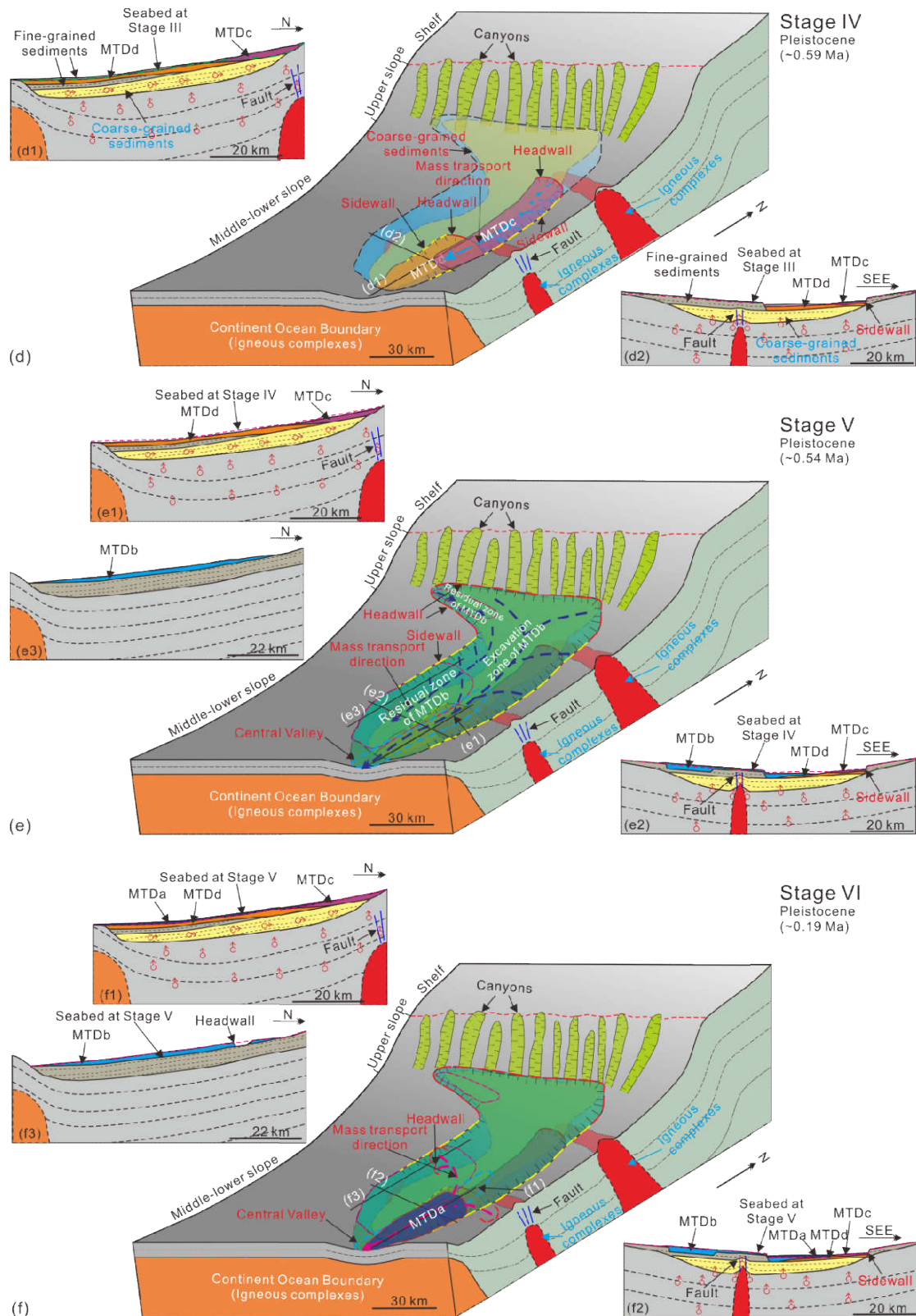
1028 Figure 12



1029

1030

1031 Figure 12 Continued



1032 (f)

1033 Figure 12: Formation processes of the repeated slope failures from middle Miocene to the end of

1034 emplacement of MTDa. (a) Stage I: In the early middle Miocene, a large long negative relief

1035 (depression) surrounded by topographic highs (massifs) had already formed; (b) Stage II: From

early middle Miocene to early Pleistocene (beginning of MTDd), turbidites transported via the slope canyons deposited on the slope from lower slope to middle slope. Coarse-grained sediments and fine-grained sediments were dominated in the early and late stages, respectively; (c) Stage III: Possibly triggered by earthquakes, MTDd formed in the lower slope; (d) Stage IV: MTDc emplaced in the middle-lower slope and eroded part of MTDd; (e) Stage V: Catastrophic MTDb involved the whole depression and evacuated most parts of the slope (only two main depositional zones could be observed); (f) Stage VI: Small-scale MTDa were probably sourced from two slope failure areas in the lower slope. Please see text for details.

1046 **Table caption**

1047 Table 1: Covering areas, thicknesses and volumes of MTDs (MTDa - MTDd) on the slope and
 1048 (MTDo1- MTDo2) in the ocean basin in this study.

	MTDa	MTDb	MTDc	MTDd	MTD_o1	MTD_o2
Area/km ²	515.25	3166	920.25	832.5	256.31	5602.72
Thickness/m	43.09	70.13	86.98	97.74	48.10	100.07
Volume/km ³	22.20	222.03	80.04	81.37	12.33	616.69

1049